Analyzing structural variations along strike in a deep-water thrust belt

Yukitsugu Totake [a,b,*], Robert W. H. Butler [a], Clare E. Bond [a], Aznan Aziz[c]

[a] Geology and Petroleum Geology, School of Geosciences, University of Aberdeen, Kings College, Aberdeen AB24 3UE, UK

[b] Technical Resources Unit, Technical Division, INPEX CORPORATION, Tokyo 107-6332, Japan

[c] Resource Exploration Department, PETRONAS, Kuala Lumpur 50088, Malaysia

*Corresponding author: yukitsugu.totake@inpex.co.jp (Y. Totake)

- Fault heave changes along strike in a deep-water thrust belt, offshore Malaysia.
- Multiple heave maxima on the main thrusts suggest merger of fault segments.
- Fault linkage sites exhibiting local heave minima concur with distributed strain on small imbricate thrusts and tight folds.
- Fault linkage and displacement kinematics are affected by adjacent structures across strike.
- A fold-thrust structure may be better characterized as a part of kinematically linked 3D system.

Abstract

We characterize a deep-water fold-thrust arrays imaged by a high-resolution 3D seismic dataset in the offshore NW Borneo, Malaysia, to understand the kinematics behind spatial arrangement of structural variations throughout the fold-thrust system. The seismic volume used covers two sub-parallel fold trains associated with a series of fore-thrusts and back-thrusts. We measured fault heave, shortening value, fold geometries (forelimb dip, interlimb angle and crest depth) along strike in individual fold trains. Heave plot on strike projection allows to identify individual thrust segments showing semi-elliptical to triangular to bimodal patterns, and linkages of these segments. The linkage sites are marked by local minima in cumulative heave. These local heave minima are compensated by additional structures, such as small imbricate thrusts and tight folds indicated by large forelimb dip and small interlimb angle. Complementary profiles of the shortening amount for the two fold trains result in smoother gradient of total shortening across the structures. We interpret this reflects kinematic interaction between two fold-thrust trains. This type of along-strike variation analysis provides comprehensive understanding of a fold-thrust system and may provide an interpretative strategy for inferring the presence of complex multiple faults in less well-imaged parts of seismic volumes.

1. Introduction

Fold-thrust belts have long been investigated in various settings, from orogenic belts to gravitational failure on passive margins, especially for the hydrocarbon exploration. In these endeavors, many interpretational strategies have been adopted in the application of structural geology. Since at least the 1980s geoscientists have developed diverse kinematic models (see Groshong et al., 2012; Brandes and Tanner, 2013 for recent reviews) and non-kinematic techniques (e.g. Williams and Chapman, 1983; Groshong and Epard, 1994) to illustrate thrust-related folding. These approaches deal with the cross-sectional geometry essentially, whereas contractional structures vary the kinematics and structural geometry along strike (Figure 1). Detailed descriptions of such along-strike structural variations remain few on thrust systems. This has led to our poor understanding of the deformation style and evolution of fold-thrust structures in three dimensions. Aims of this contribution are 1) to provide descriptions of deep-water fold-thrust arrays imaged by a high-resolution 3D seismic dataset, and 2) to assess the kinematics underlying spatial arrangement of structural variations in the fold-thrust system.

Dahlstrom (1969) demonstrated that quantitative analysis of along-strike structural variations helps explain the kinematics of a fold-thrust array in the Alberta Front Range. Based on displacement changes along strike, he postulated that a thrust fault died out laterally and the displacement lost on the thrust was transferred to another so that net shortening is largely conserved along strike (Figure 2). Dahlstrom's work has developed into various attempts to characterize structural architectures transferring displacement among thrust faults (O'Keefe and Stearns, 1982; Sanderson and Spratt, 1992; Fermor, 1999), to investigate the evolution of fold-thrust systems through the

propagation and linkage along strike (King and Yielding, 1984; Ellis and Dunlap, 1988; Nicol et al., 2002; Davis et al., 2005; Mazzoli et al., 2005), and to build geologically reasonable cross-sections throughout fold-thrust arrays (Watkins et al., 2017), with uses of variations in the shortening amount or displacement plotted on strike projections. But most studies depended on sparsely distributed data points. Few studies presented detailed characteristics of along-strike variations (Nicol et al., 2002; Davis et al., 2005). A small number of analogue experiments (Gardner and Spang, 1973; Liu and Dixon, 1991) and seismic-based studies (Higgins et al., 2009; Bergen and Shaw, 2010) have shown along-strike changes in shortening and displacement quantitatively and detailedly. The displacement distribution along strike and the kinematic linkage between thrust faults and folds are not fully resolved yet. It is mainly due to scarcity of geometrical constraints on thrust systems. Field studies suffer from the erosion removing thrust hangingwalls and the burial of footwalls beneath thrust sheets. Analogue experiments are no exception to the latter issue. Even where seismic data are available, complex seismic velocities compounded by deformation structure and repeated stratigraphy result in unclear seismic reflection images.

This contrasts with intensive studies on normal faults, where fault displacement patterns have been analyzed along strike and dip minutely in fields and with seismic datasets. Analyses of detailed displacement patterns along strike have brought significant insights into the development of fault linkage (Peacock and Sanderson, 1991; Childs et al., 1995; Dawers and Anders, 1995; Soliva and Benedicto, 2004; Giba et al., 2012), displacement-length scaling (Walsh and Watterson, 1991; Cowie and Scholz, 1992; Dawers et al., 1993; Schlische et al., 1996; Kim and Sanderson, 2005), and the fault growth history (Anders and Schlische, 1994; Cartwright et al., 1995; Jackson et al., 2002; Meyer et al., 2002; Walsh et al., 2003). Analogue experiments

have examined these works with far more detail (Mansfield and Cartwright, 2001; Bellahsen et al., 2003; Schlagenhauf et al., 2008; Wyrick et al., 2011). Advanced knowledges for normal faults may help comprehend thrust fault systems further. But we need more investigations to know how much both systems are comparable.

We describe imbricate thrusts developed through deep-water sandstone-shale sequences in the offshore area of NW Borneo, Malaysia, using a high-resolution 3D seismic dataset acquired by the multi-azimuth technology. The best quality of this 3D seismic data provides good, three-dimensional constraints for structural geometry of thrust faults and related folds. We present along-strike variations in the fault displacement, fault dip, fold geometry and shortening amount at intervals of 250 m to 1 km. Above all, the displacement variation is quantified using measurement of fault heave so that the measurement is readily made while avoiding influence of erroneous depth conversion. Using these quantified along-strike variations, we show that a single fold-thrust structure is a result of not only segment linkage along strike, but also interaction of folding and faulting, and interference with adjacent structures across strike. We provide a model accounting for spatial arrangement of structural complexity controlled by segment linkage.

2. Geological setting

The NW Borneo continental margin has been extensively explored for hydrocarbons since the 1950's (Scherer, 1980) (Figure 3a). Thanks to many industrial wells and seismic reflection surveys, the geology in this region has become clear, as summarized by various authors (e.g. Petronas, 1999; Hutchison, 2005; Cullen, 2010).

The NW Borneo continental margin is marked by regressive Middle Miocene to recent sandstone-shale successions, exceeding 11 km of thickness in some places (Lu and Shipp, 2011) (Figure 3b, c). These Neogene sediments have been shed from the Borneo interior hinterland that experienced considerable uplift and erosion from the Early Miocene onward (Morley and Back, 2008; Hall, 2013). The Neogene coastal to shallow-marine sequences unconformably overlie the Upper Cretaceous to Early Miocene deep-water accretionary prism called Rajang-Crocker Group in the inboard area (Morley et al., 2003; Sapin et al., 2011). The Neogene hemi-pelagic strata onlap the pre-Early Miocene Dangerous Ground terrane in the NW Borneo Trough (Hinz et al., 1989; Hutchison, 2010) (Figure 3b, c).

The target in this study is a fold-thrust belt developed through the Neogene deep-water successions in the slope area (Figure 3a). It is 350 km long and 70 km wide, trending NE-SW adjacent to the NW Borneo Trough. This compressional province consists of five to seven trains of fault-propagation folds associated with NW-verging thrusts (Hinz et al., 1989; Hesse et al., 2010) (Figure 3b, c). The thrust sheets are assumed to be detached on over-pressured Early Miocene shale (Ingram et al., 2004). The master detachment is estimated to lie at a depth of c. 4 km below seabed near the toe thrust front and c. 10 km at the up-slope shelf break (Morley, 2007; Morley et al., 2014). Folding and thrusting were initiated in the Late Miocene and have propagated NW-ward over time (Franke et al., 2008; Sapin et al., 2013). The process appears to continue today, as indicated by the seafloor deformation and GPS motion records (Simons et al., 2007). Note that the fold structures and their underlying thrusts were not active in a strict sequence. Although the age of growth strata indicates a general forward migration of deformation, structures were active in parallel. It is a feature to which we shall return at the end of this paper.

There are two end-member hypotheses as to the mechanism of the Neogene-to-recent compression: crustal shortening driven by collisional plate tectonics (Hinz et al., 1989) and the gravitational failure analogous to that in the Niger Delta (Tan and Lamy, 1990; Hazebroek and Tan, 1993). Many workers argued that both mechanisms have contributed, to varying degrees in terms of which is dominant (e.g. Ingram et al., 2004; Franke et al., 2008; Morley et al., 2008, 2011; Hesse et al., 2009; Sapin et al., 2013). But, these debates do not affect our structural interpretation essentially.

3. Database

The database for this study consists of data from four boreholes tied into a 3D seismic survey of c. 830 km^2 full-fold area (Figure 4). The seismic survey was acquired in 2012 using deep-towed dual-sensor broadband system of PGS GeoStreamer® and multi-azimuth technology. Data recording in structurally complex areas were repeated along three sail-line orientations at 60° to each other (Figure 4a). The multi-azimuth datasets were processed using Kirchhoff pre-stack depth migration and were then stacked through multi-survey regularization and binning. In the processed data, spacing in both inlines and crosslines is 12.5 m, sampling rate is 2 ms, and the data record length is 7 s. The vertical resolution of the data varies from c. 10 m near the sediment surface to c. 30 m at the top of deformed successions considered here, dropping to perhaps as much as 90 m at the base of these intervals. The seismic full-fold volume is covered by seismic velocities that were finalized through five iterations of velocity picking on 50 m × 50 m × 50 m (x, y and z) grid with applications of isotropic and anisotropic tomography.

4. Seismic interpretation

The seismic data clearly display multi-layered reflectors of turbiditic sandstone-shale alternations deformed into fold-thrust structures (Figure 5). These sequences interbed with seismically chaotic packages that denote cyclic occurrences of mass transport deposits, or MTDs (Algar et al., 2011) (Figure 5). A well shows that reflective packages on seismic images correspond to sand-dominant sequences and poorly reflective intervals including MTDs are shale-dominant (Figure 6). Based on structural patterns of these excellent illuminations, we identified three tectonic sequences (Figure 5b):

1) Pre-kinematic strata that show a constant stratigraphic thickness and are deformed by folds and thrusts. This unit is characterized by laterally continuous reflectors and extensive MTDs throughout the survey area. Deeper sections in thrust footwalls appear to thicken perhaps due to the drag along thrust faults.
2) Syn-kinematic strata that exhibit significant short-range changes in thickness. They thin toward anticline crests and show local onlaps within the strata and onto the pre-kinematic strata. Thrust faults cut the deeper section of the strata. Tilting angle of fold limbs decreases upward so that anticline shapes broaden at shallower depth. MTDs are not extensive as those in the pre-kinematic strata, they are distributed only on forelimbs. Extensional normal faults develop though the strata on anticline crests with minor offsets.

3) Post-kinematic strata that drape underlying deformed strata with rather constant thickness. These strata are offset by a series of minor normal faults on anticline crests, like the syn-kinematic strata.

Thrust faults are mappable from offsets in the section below the lower syn-kinematic strata. However, the deeper section, including detachment layers and ramps, are not imaged clearly.

We mapped eight regional stratigraphic markers defined at wells, seabed and horizon h8 to h2, over the seismic volume (Figure 5b, 6). These horizons interpreted are dated between Late Miocene to Quaternary based on biostratigraphic analysis (Figure 6). We also mapped horizon h1, a continuous reflector having a positive acoustic impedance at the base of the multi-layered pre-kinematic successions. This horizon is not penetrated by the wells within the seismic volume. The interval between the seabed and horizon h7 is the post-kinematic, horizons h7 to h4 define the syn-kinematic, and below horizon h4 is the pre-kinematic strata (Figure 5b). Thrust faults were interpreted along dip sections at interval of 312.5 to 1250 m and checked for spatial continuities and structural relationships to other faults and horizons on arbitrary time slices. We depth-converted horizons and thrust faults interpreted using seismic velocities calibrated with borehole data.

The mapped seismic horizons are involved in three separate, sub-parallel trains of non-cylindrical conical fold with strike trending NS to NE-SW (Figure 7). We name these fold trains A, B and C from west to east for convenience. They are mostly fault-propagation folds that are associated with underlying thrusts. Syn-kinematic horizon h7 produces relatively gentle fold shapes with the fold train B opening southward (Figure 7a), whereas pre-kinematic horizon h4 exhibits clear fold shapes cut by a

series of thrusts (Figure 7b). Individual fold trains exhibit along-strike change in geometry that may be linked to the underlying thrust geometry.

5. Methods

We describe the fold trains A and B that are well covered by the seismic data, with focus on structural variations along strike on top pre-kinematic strata, horizon h4, using the elevation map and a series of seismic profiles. The fold train C is not analyzed in this study due to its limited extent within the seismic data coverage. We then compare these observations with along-strike changes in measurements of structural geometries and kinematics - fault heave, shortening value, fault dip, forelimb dip, interlimb angle and fold crestal depth (Figure 8). All these measurements were made in depth domain after performing depth conversion.

We use the fault heave as a proxy for fault displacement (*h* in Figure 8). This is to demonstrate a practicality of the heave for analyzing displacement distribution along traces of thrust faults in the seismic-based study. Unlike normal faults frequently analyzed using throw, thrust faults are better described using heave as they incline at low angles and their horizontal displacement components are significant. Use of the heave is also advantageous in seismic studies; heave measurements are less susceptible to the seismic depth conversion. We measured fault heaves at horizon h4, on dip sections spaced every 250 m. We note that these heave measurements are sensitive to, not only fault displacements, but also fault dip angles. Relationship between fault heaves, dip-separations and fault dips in our study area shows that ratio of heave to dip-separation falls, down to near 50 % at minimum, as the fault dip

219 increases (Figure 9). This suggests that we need to analyze heave measurements
220 carefully when fault dip angles are large, as heaves become apparently diminished
221 even with constant or increased fault displacements. We deal with this by examining
222 along-strike changes in the fault dip together when we evaluate heave profiles.
223 However, majority of our heave measurements (90 % of the measurements) are
224 associated with thrusts dipping 40° or less (Figure 9). On these thrusts, heaves equal
225 more than 77 % of dip-separations that roughly correspond to fault displacements on
226 the dip sections. Most thrusts do not change their dips considerably throughout the
227 study area. Thus, we argue that overall tendencies of our heave measurements along
228 strike mostly represent those of lateral displacement patterns.

229 We calculated the shortening amount for the horizon h4, using the line-length
230 balance (Dahlstrom, 1969) (Figure 8), on dip sections spaced at 1 km intervals along
231 strike. We pinned these sections away from fold-thrust structures at hinge point of
232 synclines in thrust footwalls or place where the seismic marker becomes horizontal.
233 Shortening values are obtained by subtracting section width (*A* in Figure 8) from
234 cumulative bed length of folded and faulted horizon h4 (*B* in Figure 8) between the pin
235 lines. Note that shortening calculated by this informs total shortening accommodated
236 by faulting and folding, and excludes a component of layer-parallel shortening (such
237 as lateral compaction). The calculated shortening could contain uncertainty arising
238 from vertical compaction and choice of depth conversion. We estimate errors in the
239 shortening are +/- 8 % at maximum, based on multiple parameter tests for the
240 decompaction and depth conversion. This uncertainty is acceptable for our primary
241 purpose that is analysis of along-strike variation rather than of absolute measurement
242 values.

Finally, we measured the forelimb dip, interlimb angle and depth of anticline crests at horizon h4 (Figure 8). The forelimb dip and interlimb angle were determined on dip sections spaced at every 1 km, the fold crest depth was measured at every 250 m along fold lengths. We use these measurements to quantify variations in fold tightness and amplitude along strike. Again, up to 15 % errors caused by depth conversion could be included in the measurements of forelimb dip and interlimb angle, and 3 % errors are estimated in the crestal line depth. But overall tendencies of along-strike variations in these measurements should not be affected critically by this uncertainty, as an impact of the depth conversion choice is rather uniform over the study area.

6. Results

6.1. Observation of along-strike variations

6.1.1. *Structural pattern in map view*

On horizon h4, the fold train A extends c. 35 km along strike within the seismic area and runs northeast beyond the seismic data coverage (Figure 7Figure 6b). The fold train B is c. 48 km long, has a crest line forming a gentle arc bowed towards the northwest on the map view (Figure 7b). They are widely spaced, at 7-8 km, in the northern section, whereas the fold trains become closer, 3-5 km distance, in the central section.

Within the mapped segment, the fold train A shows a main culmination plunging southward. This fold train is associated with five fore-thrusts dipping E to SE (FA1,

FA4, FA5, FA6 and FA8) and three oppositely dipping back-thrusts (FA2b, FA3b and FA7b). Some pop-up structures (Butler, 1982) carried by these conjugate thrusts lie along the fold length (e.g. between thrusts FA1 and FA2b). The longest fore-thrust FA4 exhibits a sigmoidal fault trace in the map view whereas the other thrusts display straight or gently bowed traces (Figure 7b). This 'master thrust' (FA4) overlaps the other fore-thrusts (FA5, FA6) in the northern section where it lies within an array of imbricate thrusts (Shaw et al., 1999) (Figure 7b). Thrust FA1 is the only fore-thrust structure that is geometrically isolated from the aligned fore-thrust array on horizon h4. The thrust FA1 forms a relay pattern with the thrust FA4, exhibiting so-called soft linkage (in the sense of Walsh and Watterson, 1991). Above the relay structure there is a deflection in the fold crest line (Figure 7b).

The fold train B has two elevation culminations in the central and the northern sections and plunges away to both northeast and south (Figure 7b). The structure contains four fore-thrusts (FB1, FB2, FB3 and FB7) and three back-thrusts (FB4b, FB5b and FB6b). A pop-up structure occurs between conjugate thrusts FB3, FB4b and FB7. The fore-thrust FB1, the largest fault in the study area, has a semi-sigmoidal curvature in map view (Figure 7b), like the master thrust FA4 in the fold train A. The thrust FB1 overlaps all the fore-thrusts along the fold train B to form part of an imbricate thrust array (Figure 7b). Thrusts FB1 and FB7 form a weakly overlapping relay pattern near the northern end of the fold train (Figure 7b). Unlike the fold train A displaying kinks in the fold crest line, the fold train B exhibits a smoother anticline crest line.

6.1.2. *Cross-sectional geometries*

293 The seismic sections across the fold trains illustrate the change in fold and thrust
294 geometry along strike (Figure 10). The fold train A shows a low-amplitude kink fold
295 associated with a single fore-thrust FA1 near the southern end (Figure 10b). To the
296 north, the fold changes to tight geometry, more fore- and back-thrusts cut the syn- and
297 pre-kinematic sequences below horizon h5 (Figure 10c). The thrust FA1 terminates
298 and is replaced by the master thrust FA4, the fold becomes asymmetric and verges
299 westward (Figure 10d). The fore-thrust FA1 and back-thrust FA2b and FA3b are not
300 clearly inked to the master thrust FA4 on the seismic image (Figure 10d). The north
301 side of the soft linkage zone between thrusts FA1 and FA4, where the master thrust
302 FA4 forms the embayment trace direction to west, thrust FA4 shows significant
303 displacement associated with a gentle overlying fold geometry (Figure 7b and Figure
304 10e). Further to the north, the fold is tightened and more imbricate sheets are
305 developed around the structural culmination along with the back-thrust FA7b (Figure
306 7b and Figure 10f-h). Structurally upper imbricate sheets appear to be younger than
307 underlying sheets, creating a similar structure to ‘break-backward imbricate structure’
308 (Shaw et al., 1999), as upper sheets deform stratigraphically younger horizons in the
309 syn-kinematic sequences (e.g. Figure 10g). Back-thrusts show minor displacements
310 compared to fore-thrusts across the fold train A.
311 The fold train B evolves from near its southern end from an asymmetric, low-
312 amplitude fold verging westward on a single fore-thrust fault FB1 with significant fault
313 displacement (Figure 10a). To the north, more thrusts cut section below horizon h5
314 while the fold shape becomes tight (Figure 10b-e). The thrust FB2 appears to form an
315 isolated segment away from the master thrust FB1 at its southern end (Figure 10b).
316 These structural patterns mimic those of the fold train A described above, and the
317 geometrical changes along strike are accompanied by a decrease in fault

displacement and fault spacing. Analogous to the thrust sequence in the fold train A, upper imbricate thrusts seem to be younger than those below, based on fold deformation in syn-kinematic strata (e.g. Figure 10b, e). In the central section, where one of the fold culminations is located, the fold train B exhibits a symmetric fold shape (Figure 10f). On the north side of this culmination, the fault trace of thrust FB1 bows out to the northwest, the thrust FB1 increases its displacement and accompanies back-thrust FB4b. In accordance with these changes in fault geometry and displacement, the fold evolves to a gentle shape verging east-southeast (Figure 10g). In the northernmost section, where another culmination of the fold train occurs, thrust FB1 reduces offset while accompanying closely spaced thrust faults above (Figure 10h). The anticline here shows a tight geometry. Fault displacements accommodated by back-thrusts are minor in comparison with those of fore-thrusts as described for the fold train A.

6.2. Heave profiles

Individual thrust faults associated with the fold trains A and B show irregular shapes of heave profiles on a strike projection (Figure 11b, 12b), analogous to displacement-distance graph for normal faults. Each heave-distance profile, varying from quasi-elliptical to triangular to bimodal in shape, exhibits single or two heave maxima and diminishes to seismically undetectable heaves at the fault trace ends. Note that complete heave profiles of some thrusts (FA5, FA6, FA7b, FA8, FB6b and FB7) are uncertain, as they extend beyond the seismic area. Thrust FB2 shows large fault heave at the northern end of the trace (Figure 12b). This is because the thrust gets

close to the upper imbricate thrust FB3, and fault heave on the thrust FB2 becomes seismically unresolvable. Due to this ‘fault merger’ interpreted below the seismic resolution, the thrust FB3 shows sharply increased fault heave (Figure 12b).

The most characteristic patterns of the heave profiles are bimodal shapes associated with the master fore-thrusts, FA4 and FB1 (Figure 11b, 12b). Such uniquely shaped heave profiles do not result from changes in fault dip (Figure 11c, 12c); although the thrust FB1 slightly increases fault dips (29-35°) at its central section where fault heave is diminished, the heave pattern keeps its bimodal shape even if the fault dip effect (heave reduction at c. 20 %) is removed. These bimodal heave patterns can be explained by the merger of at least two fault segments initiated separately and propagated laterally to coalesce (Ellis and Dunlap, 1988; Liu and Dixon, 1991). Heave maxima of the master thrusts, e.g. at 23 km and 35 km along strike for FA4 (Figure 11b), indicate places where thrust segments were initiated. These locations correspond to the points in which gentle folds occur and fault traces form westward bow-shapes (Figure 11a, 12a), probably because the faulting played more important role as to the accommodation of shortening than folding there. Local heave minima in the centers of these fault traces, at 28-30 km for FA4 and 22-27 km for FB1 along strike (Figure 11b, 12b), are thought to be the sites of former fault linkage (Ellis and Dunlap, 1988). These previous linkage sites coincide with heave peak(s) of imbricate thrust(s) overlying the master thrusts, such as FA5, FB3 and perhaps FB2 (Figure 11b, 12b). Given that imbricate thrusts are relatively younger than master thrusts as we described above, these imbricate thrusts appear to be initiated selectively in the fault linkage sites to compensate for the heave deficits on the master thrusts. Nevertheless, these former linkage sites are still marked by decreases in summed heave for each fold train (Figure 11b, 12b).

368 Soft linkage sites between thrusts, at 19 km in fold train A and at 40 km in fold train
369 B along strike, are characterized by weakly overlapped heave profiles (Figure 11b,
370 12b). They present distinctive deficits in summed heave for individual fold trains. Near
371 these soft linkage sites, the master thrusts FA4 and FB1 show high heave gradients
372 of 0.18-0.52 (equivalent to displacement gradients of 0.22-0.56). This contrasts with
373 much of other fore-thrusts and back-thrusts presenting lower heave gradients of 0.04-
374 0.16 (displacement gradients of 0.05-0.17) at fault trace ends. These characters are
375 comparable with displacement patterns of normal fault arrays forming soft linkages
376 (e.g. Peacock and Sanderson, 1991). The high heave gradients of the master thrusts
377 suggest that restricted fault-tip propagation (Nicol et al., 1996) of the master thrusts
378 under the interaction with adjacent fault segments (Wlllemse et al., 1996; Gupta and
379 Scholz, 2000; Nicol et al., 2016).
380 As if to reflect such restricted fault growth, heave patterns change abruptly across
381 the soft linkage areas. For example, in the south of the soft linkage site in the fold train
382 A, the thrust FA1 and back-thrusts FA2b and FA3b show small heaves and semi-
383 elliptically shaped heave patterns (Figure 11b). Contrary to this, in the north, thrust
384 faults present increased heaves and irregularly shaped profiles (FA4-FA8) (Figure
385 11b). Given that irregularities in heave profile and high-heave values are produced by
386 segment linkage (Cartwright et al., 1995), the northern regime is thought to be in a
387 more advanced stage of fault growth than the southern area. Small heaves in the south
388 are partly attributed to the thrust FA1 dipping steeply at angles of 40-58° (Figure 11c).
389 However, even after the consideration of the impact of such large fault dips (heave
390 reduction by 50 % at most), thrusts FA1, FA2b and FA3b are no match for the thrusts
391 having significant heaves in the north.

As fault heave on the master thrust FA4 decreases to near zero at its northern end, structurally lowest fore-thrust FA6 increases fault heave, at 28-42 km along strike (Figure 11b). This is similar to displacement patterns of displacement transfer between relaying thrusts described in outcrops (Dahlstrom, 1969; Sanderson and Spratt, 1992; Davis et al., 2005; Mazzoli et al., 2005).

6.3. Fold strain

As we described above, anticlines carried by thrusts change from gentle to tight folds along their fold lengths. Fluctuations of forelimb dip and interlimb angle of these hangingwall anticlines represent such fold geometry changes along strike systematically (Figure 11d, 12d). The forelimb dip presents particularly rich variation, presumably due to fore-thrust faults that are predominant in the study area.

Along-strike variations of forelimb dip and interlimb angle are here used as fold tightness indexes or proxies for fold strain. They appear to complement summed heave profiles of individual fold trains in part (Figure 11b, 12b). Significant fold strain (tightened fold) represented by decreased interlimb angles (53-70°) and increased forelimb dips (57-64°) occurs at soft linkage sites where summed heave is diminished (Figure 11d, 12d). In the similar way, increased fold strain indicated by large forelimb dips (> 45°) along with moderately reduced interlimb angles (70-115°) is distributed on central hard linkages of the master thrusts, where summed heave decreases to form local minima. Some ends of fault traces also present relatively tight fold shapes shown by decreased interlimb angles and increased fault dips, e.g. the southern end of thrust FB1 at 4-8 km and northern end of thrust FB3 at 34 km along strike (Figure 12b). They might resemble a thrust dying out into a fold, which have been described in natural

417 structures since the early twentieth century (Elliott, 1976). When summation of heave
418 displays local maxima (e.g. at 23 km and 12 km along strike in the fold trains A and B,
419 respectively), low fold strain (gentle fold geometry) occurs in thrust hangingwalls with
420 large interlimb angles (106-135°) and gentle forelimb dips (18-31°) (Figure 11d, 12d).
421 This shows that fault initiation points accumulate fault slip rather than fold strain.
422 The mirror-image relations between the summed heave and the fold strain indicate
423 displacement transfer between folding and faulting (Elliott, 1976; Liu and Dixon, 1991;
424 Higgins et al., 2009). There are exceptions, however. Local maxima in summation of
425 heave are paired with high fold strain presented by high interlimb angles at c. 30-40
426 km along strike in both fold trains (Figure 11b, d, 12b, d). In the area, seismic sections
427 display highly strained structures that are associated with increased number of thrusts
428 and tightened folds (Figure 10g, h). Such significant strain may exceed an upper limit
429 where the folding can complement the faulting. Both faulting and folding may have to
430 accommodate shortening as much as they can.
431 The soft linkage site in the fold train A marks the greatest fold strain presented by
432 interlimb angles of 53-63° and forelimb dip of 57-60° in the study area (Figure 11d).
433 Given that summed heave decreases to near zero at the place, these measurements
434 may be nearly equal to a maximum strain attained by the folding mechanism at the
435 horizon h4 without faulting, as far as we can ascertain.
436 The elevations of fold crests show rather smooth profiles along strike (Figure 11e,
437 12e). They display similarities to variations in the forelimb dip and interlimb angle.
438 Increased fold strain indicated by the elevation peaks occurs when the summed heave
439 decreases, e.g. at soft linkage site between FB1 and FB7 and central section of master
440 thrust FB1. Low fold strain is expressed by saddles at places where the summation of
441 heave presents peaks, e.g. c. 24 km on the fold train A and 13 km and 35 km on the

fold train B along strike. But again, northern regime of the study area, at 30-40 km along strike, provides an exception; a crestal culmination occurs with greater summed heave in the fold train A (Figure 11e). This could result from significant strain that needs to be accommodated by both folding and faulting. Note that the crest of the fold train B has been eroded locally, inhibiting complete analysis of its crestal elevation.

6.4. Shortening in individual fold trains

Shortening is accommodated by three mechanisms theoretically: folding, faulting and layer-parallel shortening (Liu and Dixon, 1991). The shortening calculated in this study, by line-length balancing, only consists of the components associated with the folding and the faulting. Thus, if there is displacement transfer between these two mechanisms along strike as we inferred above, the shortening may reflect a result of such kinematic interaction.

In the fold train A, the shortening shows approximately linear increase to north (Figure 11b). This smooth trend of the shortening profile is obvious compared to fluctuated variations in summed heave, forelimb dip and interlimb angle along strike, especially in southern section. This indeed appears to be the product of displacement transfer between folding and faulting (Liu and Dixon, 1991; Higgins et al., 2009). Soft linkage site between thrusts FA1 and FA4 provides a good example. A peak of fold strain illustrated by the smallest interlimb angle and the greatest forelimb dip (Figure 11d) compensates cumulative heave decreased to near zero so that shortening presents smooth trend without abrupt gap (Figure 11b). In northern section, there are some deficits in shortening (at 27-31 and 36-38 km along strike) (Figure 11b). In this

area, increased fold strain indicated by reduced interlimb angle and increased forelimb dip occur, implying that the folding work at full stretch to accommodate shortening. The area is also characterized by large shortening values (> 2 km). Such significant shortening may be over capacity for the fold train A to take the shortening up smoothly along strike only using the folding and the faulting mechanisms.

The fold train B shows an irregular shape of shortening profile. Compared to highly fluctuated profile of summed heave along strike, variation in the shortening is slightly moderated (e.g. soft linkage at 40 km along strike), presumably due to fold strain compensating along-strike change in fault displacement. But, the irregular shape of the shortening profile indicates that such complementary relation between the folding and the faulting did not fully work within the fold train B to accommodate shortening along strike smoothly. Again, a reason for this could be significant shortening excessed a capacity limit of the complementary system between the folding and faulting. Or there may be another mechanism accommodating the shortening.

Difference between the shortening value and summation of heave informs a rough estimate of shortening taken up by the folding. Figure 13 shows that the shortening related to the folding varies along strike in concordance with variations in forelimb dip and interlimb angle (see Figure 11d, 12d for comparison). This fold-related shortening takes up 8-87 % of the shortening amount throughout both fold trains (Figure 13). The ratio of the fold-related shortening to the shortening amount is high at the soft linkage areas (52-87 %), it becomes moderate at the central hard linkages of master thrusts (20-42 %) and lower at the fault initiation points of master thrust segments (8-22 %). The value of fold-related shortening reaches peaks of c. 1.2 km at soft linkage sites and at places where imbricate thrust sheets occur (Figure 13), and does not exceed this level. Compared to summation of fault heave reaching 3.7 km (at 29 km along

strike in the fold train B), the maximum value of fold-related shortening seems relatively small. The places presented by maxima in the fold-related shortening are characterized by ultimately tightened folds on seismic sections (e.g. Figure 10g, h). The value of 1.2 km may therefore equal to an upper limit of shortening amount that folding can accommodate at horizon h4 in the study area. Note that the shortening amount taken up by the folding also depends on a structural depth of a layer; structurally upper layers can accommodate more shortening value geometrically.

6.5. Total heave and shortening across fold array

We have seen that individual fold trains present geometric and kinematic variations along strike due to displacement transfer between folds and thrust faults. But, displacement could be transferred from a fold-thrust train to another over few to tens kilometers (Dahlstrom, 1969; Sanderson and Spratt, 1992; Watkins et al., 2017). We now consider fault heave and shortening across both fold trains A and B to see if they demonstrate kinematic coherence.

Figure 14a shows that total heave across both fold trains is near zero at the southern end and increases to the peak of 6.7 km at c. 35 km along strike while fluctuating, and then declines to the northeast. Although the total heave profile shows some distinctive local peaks (at c. 19, 27 km along strike) and diminishes (at 10, 25 km along strike), the profile appears to become closer to a triangular shape generally. It is obvious compared to irregular shapes of summed heave profiles for individual fold trains (Figure 14a). The near linear gradient in total heave appear to be a result of the complementary relation in summed heave between the fold trains. Diminished fault

heaves of individual fold trains are paired with large heaves in another, or vice versa (e.g. 20-27 km along strike; Figure 14a). Kinematically linked fault arrays that propagate laterally produce linear displacement gradients (Cowie and Shipton, 1998; Davis et al., 2005). The fold trains A and B may demonstrate such propagating system by working together.

Total shortening across the fold trains presents much linear gradient (Figure 14b). It increases from zero at southern end to the peak of 7.4 km at 35 km along strike and then decreases toward the northeast. Smoother gradient in the total shortening is presumably attributed to the folding that accommodates shortening to complement the fluctuation in total heave. The fold train B displays irregular plateau shape in shortening profile at c. 10-40 km along strike (Figure 14b). This area corresponds to the section where the fold train A accommodates shortening. This may suggest that the fold train A took over the neighboring fold train B to accommodate shortening.

7. Discussion

7.1. A model for the kinematic linkage of thrusts

The deep-water fold-thrust belt in offshore NW Borneo described above exhibits a range of structural styles that vary along strike. Along their axes, anticlines vary from gentle open structures to tight folds. These major anticlines lie in the hangingwalls to thrusts. These in turn can vary along strike from single major splays to arrays of smaller imbricate thrusts and local back-thrusts. Fault heave profiles, displaying variations in displacement that we infer, reflect the growth and amalgamation of thrust

segments. Fold strains indicated by forelimb dip and interlimb angle react on the displacement patterns to buffer variation in shortening. Thus, neighboring and adjacent folds appear to be kinematically linked. We now build a model of the evolution of a simplified imbricate thrust system (Figure 15).

We have shown that two anticlinal fold trains, A and B, in the 3D seismic survey are defined by the large master thrusts, FA4 and FB1, respectively. These master thrusts are commonly characterized by sigmoidal fault traces in the map view and bimodal heave profiles on the strike projection. Sigmoidal thrust traces are observable in analogue experiments as a result of merger of curved thrust segments (e.g. Schreurs et al., 2016). Displacement pattern along fault traces in outcrops (e.g. Ellis and Dunlap, 1988; Peacock and Sanderson, 1991) and in an analogue experiment (Liu and Dixon, 1991) also suggest that coalescence of fault segments produces diminished displacement at linkage zones. These studies suggest that our master thrusts are the products of merger of at least two thrust segments, which initiated individually, growing together as they accumulated slip (Figure 15a). The two heave maxima correspond to the points of the nucleation of the individual segments. The central heave minima are the location of final linkage between the former discrete segments (Figure 15b). The occurrence of tight fold geometries at the points of heave minima may have their origin in strain localized in the soft linkages (Walsh and Watterson, 1991), or the transfer zones (in sense of O'Keefe and Stearns, 1982; Davis et al., 2005) (Figure 15b). These tight folds complement the heave deficits on the master thrusts, to their limit of shortening amount that the folding mechanism can accommodate. Small, younger imbricate thrusts are selectively initiated in the strained linkage zones to compensate the heave deficits of the master thrusts and to accommodate further shortening that the folding cannot accommodate any more

(Figure 15c). The final thrust geometry created in this way is smoother in three dimensions than the more sculpted forms that would result from a single linkage as the relay ramp was breached (Figure 15d). Lateral propagation of newer, straighter imbricate thrusts above the master thrust appears to create a geometry well-suited to accommodate further shortening. The propagation of such additional structures can be relatively rapid, as suggested by low heave gradients of the imbricate thrusts in the study area.

The master thrust we described here is not necessarily the earliest thrust fault developed in a structure; the master thrust FA4 appears to accommodate decreased fault displacement on the structurally lower and older thrust FA6. We assume any thrust faults can follow the steps modelled above if conditions are complete (e.g. alignment of faults), irrespective of thrust sequence. Our model may occur at multiple sites along a single fold train.

The deflection along the axis of fold train A is associated with the soft linkage area between thrusts FA1 and FA4 (Figure 15d). We assume this site of soft linkage hampered along-strike propagation of thrust array consisting of FA4, FA5 and FA6, as indicated by high heave gradient of the master thrust. The soft linkage area presents decrease in summed heave and a greater fold strain indicated by small interlimb angle and large forelimb dip. Similar relationships between fold strain and fault linkage sites have been previously inferred (Davis et al., 2005; Higgins et al., 2009). Linear gradient of shortening across the site of soft linkage suggests that the folding plays an important role to maintain the kinematic coherence across the soft linkage area instead of faulting. Given that fold strain is almost at the upper limit for accommodating shortening (c. 1.2 km), the soft linkage zone may be verging on a breach by faults to evolve to a hard linkage zone.

Relative importance of the folding in accommodating the shortening amount varies along strike, depending on the activity of thrust fault(s) and the bulk shortening. At a place where fault propagation is impeded, e.g. by the soft linkage site described above, the folding becomes principal mechanism to accommodate the shortening to compensate the decrease in fault displacement. In an area where the faulting takes up the shortening dominantly, such as fault nucleation points, the folding is less important. Under the significant amount of bulk shortening (e.g. > 2 km in our case), the folding may exert all its capacity to accommodate shortening together with the faulting. Eventually, the proportion of the shortening taken up by the folding to the bulk shortening can change in a wide range from near 0 to 100 %.

Our discussions to this point have focused on kinematic linkage of thrust segments associated with a single train of hangingwall anticline. However, our cumulative heave plots and total shortening for the two main fold trains show complementary displacement patterns and shortening profiles. Thus, these two fold-thrust systems appear to work together. Such behavior should be expected. Maximum distance at which fold-thrust structures can work together remains unknown. But, it can be more than 8 km based on the observable distance between the two fold trains. The regional cross-section (Figure 3b, c) used here to set the scene for our three-dimensional study shows that arrays of fold-thrust structures operated in parallel. They can relay between each other along axis, as predicted by Dahlstrom (1969). Therefore, the occurrence of linkage involving strain localization and imbricate thrusts is dynamically affected by adjacent structures across strike. It is misleading to treat individual fold-thrust structures in isolation.

7.2. Comparisons to fold-thrust models

Kinematic models, such as fault-bend fold (Suppe, 1983; Medwedeff and Suppe, 1997; Suppe et al., 2004), fault-propagation fold (Mitra, 1990; Suppe and Medwedeff, 1990; Mitra and Mount, 1998) and detachment fold (Epard and Groshong, 1995; Poblet and McClay, 1996; Mitra, 2002), illustrate the evolution of the thrust-related folding identified in outcrops and on seismic images while following the balancing theory. They have brought insights into the development process of fold-thrust structures and advances in the prediction of subsurface geometry. Particularly in thrust settings where seismic images are often degraded, advantages to use the kinematic models in testing structural interpretation have been well argued (Hardage et al., 1999; Shaw et al., 2005; Kostenko et al., 2008; Cardozo and Brandenburg, 2014; Malz et al., 2015).

The kinematic models are simplified and idealized templates of natural structures. They represent large-scale deformation style of the structures, but often fail to account for detailed features of structures (Butler and McCaffrey, 2004; Morley, 2009; Hardy, 2011; Torvela and Bond, 2011; Brandes and Tanner, 2013). This is particularly evident in cases where displacement is small. For example, both fault-bend fold and fault-propagation fold envisage a thrust fault propagated up-dip from a detachment fault. However, at early stage of the fault development, thrust faults can nucleate away from the detachment fault and propagate both up- and down-dip (Williams and Chapman, 1983; Kattenhorn, 1994; McConnell et al., 1997; de Vera et al., 2010; Ferrill et al., 2016; Ghisetti et al., 2016). In our study area, some of the imbricate thrusts and back-thrusts marked by small fault heaves appear to show similar characters (e.g. FB2 in Figure 10b, FA1 and FA3b in Figure 10d). Shaw et al. (1999) showed that fault-bend

642 fold models can describe a variety of imbricate structures. The kinematic models could
643 forecast such structures reasonably only if fault displacement is large enough to
644 develop a linkage between the fore-thrust segment and the detachment fault.

645 Besides, the kinematic models treat cross-sectional geometry basically.
646 Characterization of a fold-thrust structure in three dimensions by them remains
647 challenging, although there are few attempts to expand the algorithms into three
648 dimensions (Cristallini et al., 2004; Cardozo, 2008). The kinematic models may be
649 applied onto serial cross-sections arranged at certain intervals along strike so that 3-
650 D structural geometry of a structure is apparently illustrated (Wilkerson et al., 1991;
651 Rodriguez-Roa and Wiltschko, 2010). This is in fact desirable approach, because the
652 lateral compatibility of model parameters used is ensured (Watkins et al., 2017). In
653 many cases, however, project time restrictions allow to work only on selected cross-
654 sections spaced sparsely, 3-D characterization of the structures using kinematic
655 models are roughly attainable.

656 Profiles of geometrical measurements along strike can be made quickly. In this
657 study, we spent less than a day for measuring fault heave, fold limb angles, fold crest
658 depth and shortening. The measurement of fault heave can be especially speedy as
659 it does not require seismic depth conversion. The profiles of these measurements
660 inform very detailed characters of the kinematics underlying the spatial variation in
661 structural style across the structures. Eventually this approach can establish a pseudo
662 three-dimensional view of the kinematic evolution of structures. Although our model,
663 of the relationships between thrust segment linkages and structural complexity, needs
664 to be proven by other studies, if confirmed, they could help forecast structural
665 complexity on low quality seismic dataset.

Use of kinematic models in combination with analysis of along-strike variation in geometrical measurements may be the best mix. Better understanding obtained through analysis of the geometrical measurement profiles is expected to sharpen an area of interest for analysis with kinematic models, it also provides a guide for model parameters. Thus, a work with the kinematic models could be optimized. The kinematic models in turn can verify the structural geometry of seismic interpretation, and justify the kinematics inferred by the profile analysis. Such conjunction of two methodologies can lead to comprehensive understanding of the 3-D structural geometry and underlying kinematics.

8. Conclusions

Changes in structural style along two anticlinal trains in a deep-water fold-thrust belt, offshore NW Borneo, were described here using a high-resolution 3D seismic dataset. Use of along-strike profiles of fault heave, shortening and fold geometry measurements are effective for illustrating the kinematic interactions between folds and thrusts, which underlie arrangement of structural variations in the fold-thrust system.

Based on our analysis of these profiles allied to structural interpretation, we can conclude the following:

1. The large master thrusts that define the fold-thrust structures are produced by the amalgamation of two or more thrust faults. The former fault linkages are marked by local heave minima.

2. The small imbricate thrusts above the master thrust, and increased fold tightness, are spatially associated with sites of former linkage of the master thrust. These additional structures in part compensate for the deficit in heave on the master fault.
3. Folding can accommodate shortening to its limit that mainly depends on structural depth level of a stratigraphic layer. The folding mechanism compensates variation in fault displacement.
4. Adjacent structures in a thrust array can interact both along and across strike. It may be misleading to consider each structure in isolation but rather as a part of a three dimensional, kinematically linked system. It remains unclear over what length-scales these interactions can occur.

In many thrust systems, subsurface imaging is of a substantially lower quality than for the Borneo data we have used here. Consequently, forecasting subsurface structure has commonly been driven by idealized fold-thrust models (e.g. Shaw et al., 2005). This study casts doubt on this approach, as idealized models cannot fully account for structural features marked with small displacement, such as imbricate thrusts and back-thrusts. The fold-thrust models also have a limit to address along-strike structural variations because they essentially work on the cross-section parallel to the transport direction of rock deformation.

Our analysis of geometrical measurements plotted on the strike projection can be readily performed. Particularly heave profile analysis is quickly performed, as fault heave is essentially a measure of horizontal offset and does not require depth conversion. Analysis of along-strike measurement profiles is useful for investigating the kinematic coherence along and across structures. Our study shows that the zones

of greater structural complexity, as marked by greater arrays of imbricate thrusts, coincide with sites of kinematic linkage between the main thrust segments. These in turn coincide with axial deflections of the thrust hangingwall anticlines. These relationships, if confirmed by other studies, could provide useful guides for forecasting structural complexity even when seismic quality is low. Analysis of along-strike variations prior to use of a kinematic model may be beneficial, as along-strike profiles could provide a guide for areas of interest and model parameters.

Acknowledgements

This study is based on part of PhD research funded by INPEX CORPORATION at University of Aberdeen. We acknowledge Petronas for the release of beautiful images of 3D seismic data along with borehole information. We thank Schlumberger for the academic use of Petrel software. We are truly thankful to Nancye Dawers, Haakon Fossen, Roy Gabrielsen and Steve Laubach for their invaluable and constructive comments that considerably improved the manuscript.

References

Algar, S., Milton, C., Upshall, H., Roestenburg, J., Paul Crevello, 2011. Mass-Transport Deposits of the Deepwater Northwestern Borneo Margin - Characterization From Seismic-Reflection, Borehole, and Core Data With Implications for Hydrocarbon Exploration and Exploitation, in: Shipp, R.C., Weimer, P., Posamentier, H.W. (Eds.), Mass-Transport Deposits in Deepwater Settings, SEPM Special Publication 96. Society for Sedimentary Geology, Telsa, Oklahoma, pp. 351–366.

Anders, M.H., Schlische, R.W., 1994. Overlapping Faults, Intrabasin Highs, and the Growth of Normal Faults. The Journal of Geology 102, 165–180.

Bellahsen, N., Daniel, J.M., Bollinger, L., Burov, E., 2003. Influence of viscous layers on the growth of normal faults: Insights from experimental and numerical models. Journal of Structural Geology 25, 1471–1485.

Bergen, K.J., Shaw, J.H., 2010. Displacement profiles and displacement-length scaling relationships of thrust faults constrained by seismic-reflection data. Geological Society of America Bulletin 122, 1209–1219.

Brandes, C., Tanner, D.C., 2013. Fault-related folding: A review of kinematic models and their application. Earth-Science Reviews 138, 352–370.

Butler, R.W.H., 1982. The terminology of structures in thrust belts. Journal of Structural Geology 4, 239–245.

Butler, R.W.H., McCaffrey, W.D., 2004. Nature of thrust zones in deep water sand-shale sequences: outcrop examples from the Champsaur sandstones of SE France. Marine and Petroleum Geology 21, 911–921.

Cardozo, N., 2008. Trishear in 3D. Algorithms, implementation, and limitations. Journal of Structural Geology 30, 327–340.

Cardozo, N., Brandenburg, J.P., 2014. Kinematic modeling of folding above listric propagating thrusts. Journal of Structural Geology 60, 1–12.

Cartwright, J.A., Trudgill, B.D., Mansfield, C.S., 1995. Fault growth by segment linkage: an explanation for scatter in maximum displacement and trace length data from the Canyonlands Grabens of SE Utah. Journal of Structural Geology 17, 1319–1326.

Childs, C., Watterson, J., Walsh, J.J., 1995. Fault overlap zones within developing normal fault systems. Journal of the Geological Society 152, 535–549.

Cowie, P.A., Scholz, C., 1992. Displacement-length scaling relationship for faults: data synthesis and discussion. Journal of Structural Geology 14, 1149–1156.

Cowie, P.A., Shipton, Z.K., 1998. Fault tip displacement gradients and process zone dimensions. Journal of Structural Geology 20, 983–997.

771 Cristallini, E.O., Giambiagi, L., Allmendinger, R.W., 2004. True three-dimensional
772 trishear: A kinematic model for strike-slip and oblique-slip deformation. Bulletin of
773 the Geological Society of America 116, 938–952.

774 Cullen, A.B., 2010. Transverse segmentation of the Baram-Balabac Basin, NW
775 Borneo: refining the model of Borneo's tectonic evolution. Petroleum Geoscience
776 16, 3–29.

777 Dahlstrom, C.D.A., 1969. Balanced cross sections. Canadian Journal of Earth
778 Sciences 6, 743–757.

779 Davis, K., Burbank, D.W., Fisher, D., Wallace, S., Nobes, D., 2005. Thrust-fault growth
780 and segment linkage in the active Ostler fault zone, New Zealand. Journal of
781 Structural Geology 27, 1528–1546.

782 Dawers, N.H., Anders, M.H., 1995. Displacement-length scaling and fault linkage.
783 Journal of Structural Geology 17, 607–614.

784 Dawers, N.H., Anders, M.H., Scholz, C.H., 1993. Growth of normal faults:
785 Displacement-length scaling. Geology 21, 1107–1110.

786 de Vera, J., Granado, P., McClay, K., 2010. Structural evolution of the Orange Basin
787 gravity-driven system, offshore Namibia. Marine and Petroleum Geology 27, 223–
788 237.

789 Elliott, D., 1976. The Energy Balance and Deformation Mechanisms of Thrust Sheets.
790 Philosophical Transactions of the Royal Society A: Mathematical, Physical and
791 Engineering Sciences 283, 289–312.

792 Ellis, M.A., Dunlap, W.J., 1988. Displacement variation along thrust faults: implications
793 for the development of large faults. Journal of Structural Geology 10, 183–192.

794 Epard, J.-L., Groshong, R.H.J., 1995. Kinematic model of detachment folding including
795 limb rotation, fixed hinges and layer-parallel strain. Tectonophysics 247, 85–103.

796 Fermor, P., 1999. Aspects of the three-dimensional structure of the Alberta Foothills
797 and Front Ranges. Geological Society of America Bulletin 111, 317–346.

798 Ferrill, D.A., Morris, A.P., Wigginton, S.S., Smart, K.J., McGinnis, R.N., Lehrmann, D.,
799 2016. Deciphering thrust fault nucleation and propagation and the importance of
800 footwall synclines. Journal of Structural Geology 85, 1–11.

801 Franke, D., Barckhausen, U., Heyde, I., Tingay, M., Ramli, N., 2008. Seismic images
802 of a collision zone offshore NW Sabah/Borneo. Marine and Petroleum Geology
803 25, 606–624.

804 Gardner, D.A.C., Spang, J.H., 1973. Model Studies of the Displacement Transfer
805 Associated with Overthrust Faulting. Bulletin of Canadian Petroleum Geology 4,
806 534–552.

807 Ghisetti, F.C., Barnes, P.M., Ellis, S., Plaza-Faverola, A.A., Barker, D.H.N., 2016. The
808 last 2 Myr of accretionary wedge construction in the central Hikurangimargin

(North Island, New Zealand): Insights fromstructuralmodeling. Geochemistry Geophysics Geosystems 17, 2661–2686.

Giba, M., Walsh, J.J., Nicol, A., 2012. Segmentation and growth of an obliquely reactivated normal fault. Journal of Structural Geology 39, 253–267.

Groshong, R.H.J., Bond, C.E., Gibbs, A.D., Ratliff, R., Wiltschko, D. V., 2012. Preface: Structural balancing at the start of the 21st century: 100 years since Chamberlin. Journal of Structural Geology 41, 1–5.

Groshong, R.H.J., Epard, J.-L., 1994. The role of strain in area-constant detachment folding. Journal of Structural Geology 16, 613–618.

Gupta, A., Scholz, C.H., 2000. A model of normal fault interaction based on observations and theory. Journal of Structural Geology 22, 865–879.

Hall, R., 2013. Contraction and extension in northern Borneo driven by subduction rollback. Journal of Asian Earth Sciences 76, 399–411.

Hardage, B.A., Pendleton, V.M., Major, R.P., Asquith, G.B., Schultz-eia, D., Lancasterft, D.E., 1999. Case History Using petrophysics and cross-section balancing to interpret complex structure in a limited-quality 3-D seismic image. Geophysics 64, 1760–1773.

Hardy, S., 2011. Cover deformation above steep, basement normal faults: Insights from 2D discrete element modeling. Marine and Petroleum Geology 28, 966–972.

Hazebroek, H.P., Tan, D.N.K., 1993. Tertiary tectonic evolution of the NW Sabah continental margin. Bulletin of the Geological Society of Malaysia 33, 195–210.

Hesse, S., Back, S., Franke, D., 2010. Deepwater folding and thrusting offshore NW Borneo, SE Asia. Geological Society, London, Special Publications 348, 169–185.

Hesse, S., Back, S., Franke, D., 2009. The deep-water fold-and-thrust belt offshore NW Borneo: Gravity-driven versus basement-driven shortening. Geological Society of America Bulletin 121, 939–953.

Higgins, S., Clarke, B., Davies, R.J., Cartwright, J., 2009. Internal geometry and growth history of a thrust-related anticline in a deep water fold belt. Journal of Structural Geology 31, 1597–1611.

Higgins, S., Davies, R.J., Clarke, B., 2007. Antithetic fault linkages in a deep water fold and thrust belt. Journal of Structural Geology 29, 1900–1914.

Hinz, K., Fritsch, J., Kempter, E.H.K., Mohammad, a. M., Meyer, J., Mohamed, D., Vosberg, H., Weber, J., Benavidez, J., 1989. Thrust tectonics along the north-western continental margin of Sabah/Borneo. Geologische Rundschau 78, 705–730.

Hutchison, C.S., 2010. The North-West Borneo Trough. Marine Geology 271, 32–43.

Hutchison, C.S., 2005. Geology of North-West Borneo: Sarawak, Brunei and Sabah,

First. ed. Elsevier.

Ingram, G.M., Chisholm, T.J., Grant, C.J., Hedlund, C.A., Stuart-Smith, P., Teasdale, J., 2004. Deepwater North West Borneo: hydrocarbon accumulation in an active fold and thrust belt. Marine and Petroleum Geology 21, 879–887.

Jackson, C.A.-L., Gawthorpe, R.L., Sharp, I.R., 2002. Growth and linkage of the East Tanka fault zone, Suez rift: structural style and syn-rift stratigraphic response. Journal of the Geological Society 159, 175–187.

Kattenhorn, S.A., 1994. Outcrop-scale fault-related folds, Valley and Ridge Province, Appalachians: comparison to kinematic model predictions. The University of Akron.

Kim, Y.-S., Sanderson, D.J., 2005. The relationship between displacement and length of faults: a review. Earth-Science Reviews 68, 317–334.

King, G., Yielding, G., 1984. The evolution of a thrust fault system: processes of rupture initiation, propagation and termination in the 1980 El Asnam (Algeria) earthquake. Geophysical Journal of the Royal Astronomical Society 77, 915–933.

Kostenko, O. V., Naruk, S.J., Hack, W., Poupon, M., Meyer, H.-J., Mora-Glukstad, M., Anowai, C., Mordi, M., 2008. Structural evaluation of column-height controls at a toe-thrust discovery, deep-water Niger Delta. American Association of Petroleum Geologists Bulletin 92, 1615–1638.

Liu, S., Dixon, J.M., 1991. Centrifuge modelling of thrust faulting: structural variation along strike in fold-thrust belts. Tectonophysics 188, 39–62.

Lu, H., Shipp, R.C., 2011. Impact of a Large Mass-Transport Deposit on a Field Development in the Upper Slope of Southwestern Sabah, Malaysia, Offshore Northwest Borneo, in: Mass-Transport Deposits in Deepwater Settings, SEPM Special Publication 96. pp. 199–218.

Malz, A., Madritsch, H., Kley, J., 2015. Improving 2D seismic interpretation in challenging settings by integration of restoration techniques : A case study from the Jura fold-and-thrust belt. Interpretation 3, SAA37–SAA58.

Mansfield, C., Cartwright, J., 2001. Fault growth by linkage: Observations and implications from analogue models. Journal of Structural Geology 23, 745–763.

Mazzoli, S., Pierantoni, P.P., Borraccini, F., Paltrinieri, W., Deiana, G., 2005. Geometry, segmentation pattern and displacement variations along a major Apennine thrust zone, central Italy. Journal of Structural Geology 27, 1940–1953.

McConnell, D.A., Kattenhorn, S.A., Benner, L.M., 1997. Distribution of fault slip in outcrop-scale fault-related folds, appalachian mountains. Journal of Structural Geology 19, 257–267.

Medwedeff, D.A., Suppe, J., 1997. Multibend fault-bend folding. Journal of Structural Geology 19, 279–292.

884 Meyer, V., Nicol, A., Childs, C., Walsh, J.J., Watterson, J., 2002. Progressive
885 localisation of strain during the evolution of a normal fault population. Journal of
886 Structural Geology 24, 1215–1231.

887 Mitra, S., 2002. Structural models of faulted detachment folds. American Association
888 of Petroleum Geologists Bulletin 86, 1673–1694.

889 Mitra, S., 1990. Fault-Propagation Folds: Geometry, Kinematic Evolution, and
890 Hydrocarbon Traps (1). American Association of Petroleum Geologists Bulletin
891 74, 921–945.

892 Mitra, S., Mount, S. Van, 1998. Foreland basement-involved structures. AAPG Bulletin
893 82, 70–109.

894 Morley, C.K., 2009. Geometry of an oblique thrust fault zone in a deepwater fold belt
895 from 3D seismic data. Journal of Structural Geology 31, 1540–1555.

896 Morley, C.K., 2007. Interaction between critical wedge geometry and sediment supply
897 in a deep-water fold belt. Geology 35, 139.

898 Morley, C.K., Back, S., 2008. Estimating hinterland exhumation from late orogenic
899 basin volume, NW Borneo. Journal of the Geological Society 165, 353–366.

900 Morley, C.K., Back, S., Van Rensbergen, P., Crevello, P., Lambiase, J.J., 2003.
901 Characteristics of repeated, detached, Miocene-Pliocene tectonic inversion
902 events, in a large delta province on an active margin, Brunei Darussalam, Borneo.
903 Journal of Structural Geology 25, 1147–1169.

904 Morley, C.K., King, R., Hillis, R.R., Tingay, M., Backé, G., 2011. Deepwater fold and
905 thrust belt classification, tectonics, structure and hydrocarbon prospectivity: A
906 review. Earth-Science Reviews 104, 41–91.

907 Morley, C.K., Tingay, M., Hillis, R.R., King, R., 2008. Relationship between structural
908 style, overpressures, and modern stress, Baram Delta Province, northwest
909 Borneo. Journal of Geophysical Research 113, 1–23.

910 Morley, C.K., Warren, J., Tingay, M., Boonyasaknanon, P., Julapour, A., 2014.
911 Comparison of modern fluid distribution, pressure and flow in sediments
912 associated with anticlines growing in deepwater (Brunei) and continental
913 environments (Iran). Marine and Petroleum Geology 51, 210–229.

914 Nicol, A., Childs, C., Walsh, J.J., Manzocchi, T., Scho, M.P.J., Hutt, L., Zealand, N.,
915 Group, F.A., 2016. Interactions and growth of faults in an outcrop-scale system.
916 The Geological Society of London Special Publication 439.

917 Nicol, A., Gillespie, P.A., Childs, C., Walsh, J.J., 2002. Relay zones between
918 mesoscopic thrust faults in layered sedimentary sequences. Journal of Structural
919 Geology 24, 709–727.

920 Nicol, A., Watterson, J., Walsh, J.J., Childs, C., 1996. The shapes, major axis
921 orientations and displacement patterns of fault surfaces. Journal of Structural
922 Geology 18, 235–248.

O'Keefe, F.X., Stearns, D.W., 1982. Characteristics of displacement transfer zones associated with thrust faults, in: Geologic Studies of the Cordilleran Thrust Belt. pp. 219–233.

Peacock, D.C.P., Sanderson, D.J., 1991. Displacement, segment linakge and relay ramps in normal fault zones. Journal of Structural Geology 13, 721–733.

Petronas, 1999. The Petroleum Geology and Resources of Malaysia. Petroliam Nasional Berhad (PETRONAS), Kuala Lumpur.

Poblet, J., McClay, K., 1996. Geometry and Kinematics of Single-Layer Detachment Folds. American Association of Petroleum Geologists Bulletin 80, 1085–1109.

Rodriguez-Roa, F.A., Wiltschko, D. V., 2010. Thrust belt architecture of the central and southern Western Foothills of Taiwan. Geological Society, London, Special Publications 348, 137–168.

Sanderson, D.A., Spratt, D.A., 1992. Triangle zone and displacement transfer structures in the eastern Front Ranges, southern Canadian Rocky Mountains. American Association of Petroleum Geologists Bulletin 76, 828–839.

Sapin, F., Hermawan, I., Pubellier, M., Vigny, C., Ringenbach, J.-C., 2013. The recent convergence on the NW Borneo Wedge - a crustal-scale gravity gliding evidenced from GPS. Geophysical Journal International 193, 549–556.

Sapin, F., Pubellier, M., Lahfid, A., Janots, D., Aubourg, C., Ringenbach, J.-C., 2011. Onshore record of the subduction of a crustal salient: example of the NW Borneo Wedge. Terra Nova 23, 232–240.

Scherer, F.C., 1980. Exploration in East Malaysia of the past decade. Giant Oil and Gas Fields of the Decade 1968-1978 30, 423–440.

Schlagenhauf, A., Manighetti, I., Malavieille, J., Dominguez, S., 2008. Incremental growth of normal faults: Insights from a laser-equipped analog experiment. Earth and Planetary Science Letters 273, 299–311.

Schlische, R.W., Young, S.S., Ackermann, R. V., Gupta, A., 1996. Geometry and scaling relations of a population of very small rift-related normal faults. Geology 24, 683–686.

Schreurs, G., Buiter, S.J.H., Boutelier, J., Burberry, C., Callot, J.P., Cavozzi, C., Cerca, M., Chen, J.H., Cristallini, E., Cruden, A.R., Cruz, L., Daniel, J.M., Da Poian, G., Garcia, V.H., Gomes, C.J.S., Grall, C., Guillot, Y., Guzm??n, C., Hidayah, T.N., Hilley, G., Klinkm??ller, M., Koyi, H.A., Lu, C.Y., Maillot, B., Meriaux, C., Nilfouroushan, F., Pan, C.C., Pillot, D., Portillo, R., Rosenau, M., Schellart, W.P., Schlische, R.W., Take, A., Vendeville, B., Vergnaud, M., Vettori, M., Wang, S.H., Withjack, M.O., Yagupsky, D., Yamada, Y., 2016. Benchmarking analogue models of brittle thrust wedges. Journal of Structural Geology 92, 116–139.

Shaw, J.H., Bilotti, F., Brennan, P.A., 1999. Patterns of imbricate thrusting. Bulletin of the Geological Society of America 111, 1140–1154.

962 Shaw, J.H., Connors, C.D., Suppe, J., 2005. Structural interpretation methods, in:
963 Seismic Interpretation of Contractional Fault-Related Folds, An AAPG Seismic
964 Atlas. pp. 2–58.

965 Simons, W.J.F., Socquet, A., Vigny, C., Ambrosius, B.A.C., Abu, S.H., Promthong, C.,
966 Subarya, C., Sarsito, D.A., Matheussen, S., Morgan, P., Spakman, W., 2007. A
967 decade of GPS in Southeast Asia: Resolving Sundaland motion and boundaries.
968 Journal of Geophysical Research: Solid Earth 112, 1–20.

969 Soliva, R., Benedicto, A., 2004. A linkage criterion for segmented normal faults.
970 Journal of Structural Geology 26, 2251–2267.

971 Suppe, J., 1983. Geometry and kinematics of fault-bend folding. American Journal of
972 Science 283, 684–721.

973 Suppe, J., Connors, C.D., Zhang, Y., 2004. Shear Fault-bend Folding, in: McClay, K.R.
974 (Ed.), Thrust Tectonics and Hydrocarbon Systems: AAPG Memoir 82. American
975 Association of Petroleum Geologists, pp. 303–323.

976 Suppe, J., Medwedeff, D.A., 1990. Geometry and kinematics of fault-propagation
977 folding. Eclogae Geologicae Helvetiae 454, 409–454.

978 Tan, D.N.K., Lamy, J.M., 1990. Tectonic evolution of the NW Sabah continental margin
979 since the Late Eocene. Geological Society of Malaysia, Bulletin 27, 241–260.

980 Torvela, T., Bond, C.E., 2011. Do experts use idealised structural models? Insights
981 from a deepwater fold–thrust belt. Journal of Structural Geology 33, 51–58.

982 Walsh, J.J., Bailey, W.R., Childs, C., Nicol, A., Bonson, C.G., 2003. Formation of
983 segmented normal faults: A 3-D perspective. Journal of Structural Geology 25,
984 1251–1262.

985 Walsh, J.J., Watterson, J., 1991. Geometric and kinematic coherence and scale
986 effects in normal fault systems. Geological Society, London, Special Publications
987 56, 193–203.

988 Watkins, H., Butler, R.W.H., Bond, C.E., 2017. Using laterally compatible cross
989 sections to infer fault growth and linkage models in foreland thrust belts. Journal
990 of Structural Geology 96, 102–117.

991 Wilkerson, S.M., Medwedeff, D.A., Marshak, S., 1991. Geometrical modeling of fault-
992 related folds: a pseudo-three-dimensional approach. Journal of Structural
993 Geology 13, 801–812.

994 Williams, G., Chapman, T., 1983. Strains developed in the hangingwalls of thrusts due
995 to their slip/propagation rate: A dislocation model. Journal of Structural Geology
996 5, 563–571.

997 Wlllemse, E.J.M., Pollard, D.D., Aydin, A., 1996. Three-dimensional analyses of slip
998 distributions on normal fault arrays with consequences for fault scaling. Pergamon
999 Journal of Structural Geology 18, 295–309.

1000 Wyrick, D.Y., Morris, A.P., Ferrill, D.A., 2011. Normal fault growth in analog models
1001 and on Mars. Icarus 212, 559–567.

1002

Figure captions

Figure 1. Examples of along-strike variation on fold-thrust structures. (a) A thrust fault dying out into a fold (modified from Elliott, 1976). (b) Change in vergence direction along strike on a fold-thrust structure in Deep-water Niger Delta (after Higgins et al., 2007)

Figure 2. Displacement transfer model by Dahlstrom (1969) in the Alberta Front Range of the Canadian Cordillera. (a) Simplified serial cross-sections of a thrust array (modified from Dahlstrom, 1969). i, ii and iii are thrust faults. (b) Fault displacement plotted against along-strike distance. As displacements on individual thrusts decrease laterally, displacements on another thrusts increase, subsequently total displacement is largely unchanged.

Figure 3. Location map and regional 2D seismic profile of offshore Northwest Borneo. (a) Regional tectonic map of the offshore area of Northwest Borneo. Inset shows map location in Southeast Asia. Fault map is modified from Cullen (2010) and is superimposed on the Shuttle Radar Topography Mission Digital Elevation Model. Dashed line shows bathymetric contours at the interval of 500 m. Filled gray rectangle is location of 3D seismic data used in this study. (b) Regional 2D seismic profile of “Line A” and (c) a structural interpretation of the seismic profile. Profiles are displayed at no vertical exaggeration with an assumption of the average seismic velocity of 2.7 km/s. Principal unconformities are labelled on the horizons; SCSU = South China Sea Unconformity (Early Miocene), M/P = Miocene-Pliocene boundary (~5.3 Ma), L/UP =

Lower/Upper Pliocene boundary (~3.6 Ma) and P/Q = Pliocene/Quaternary boundary (~1.8 Ma).

Figure 4. Perspective view of 3D seismic survey with (a) syn-kinematic horizon h7, and (b) top pre-kinematic horizon h4. Two-way arrows show sail-line orientations of multi-azimuth survey. Translucent planes with dashed border lines are location of a dip section shown in Figure 5. Four wells (Well 1 to 4) were tied into seismic survey with sonic logs and check shot surveys. Only seismic volume within full-fold area is displayed. Elevation of horizons is displayed in two-way time with contour interval of 100 ms. The survey location is in Figure 3.

Figure 5. A dip profile of 3D seismic survey. (a) Uninterpreted and (b) interpreted seismic profile. Multi-layered reflectors of turbiditic sequences interbed with seismically chaotic mass transport deposits. Pre-, Syn- and Post-kinematic strata are identified based on structural patterns. White rectangle shows area of Figure 6. Location of the profile is shown in Figure 4. Profiles are displayed at no vertical exaggeration with an assumption of the average seismic velocity of 2.7 km/s.

Figure 6. Correlation between gamma-ray log response and seismic character at Well 3 location. Low gamma-ray, sandy sequences correspond with reflective packages while high gamma-ray, shaly intervals match with less reflective characters on seismic image. Formation ages presented alongside the profile are based on biostratigraphic analysis. See Figure 4, 5 for profile location. The profile has no vertical exaggeration with an assumption of the average seismic velocity of 2.7 km/s.

Figure 7. Elevation maps of key seismic horizons. (a) Syn-kinematic horizon h7. (b) Top Pre-kinematic horizon h4. Red lines with triangles show trace of fore-thrusts and orange lines with triangles are of back-thrusts in the hangingwalls. Major thrusts are labelled. White diagonal crosshatch indicates area of erosions on fold crest. Lines a to h are locations of seismic profiles in Figure 10. Contour interval is 100 m.

Figure 8. Diagram of structural geometry measured for quantifying along-strike variations on fold-thrust structures. h: fault heave, α: forelimb dip, β: interlimb angle, γ: fault dip, A: width of section, B: bed length. A subtracted from B leaves approximate estimate of the shortening amount.

Figure 9. Relationship between fault heave, dip-separation and fault dip angle. Measurements only for thrusts with significant displacements are plotted (FA1, FA4, FA5, FA6, FA7b, FA8, FB1, FB2, FB3, FB4b, FB7). As fault dip increases, difference between fault heave and dip-separation increases.

Figure 10. Selected seismic sections perpendicular to fold trains. Locations of sections are shown in Figure 7. Profiles are displayed at approximately no vertical exaggeration with an assumption of the average seismic velocity of 2.7 km/s. Major thrust faults are labelled. High-resolution images are provided in the Supplemental Materials.

Figure 11. Along-strike variations of the fold train A on strike projection. (a) Depth map of horizon h4 with thrust fault traces. Contour interval is at 100 m. (b) Fault heave and shortening value, (c) Fault dip angle for selected thrusts, (d) forelimb dip and interlimb angle, and (e) Depth to fold crest of horizon h4.

Figure 12. Along-strike variations of the fold train B on strike projection. (a) Depth map of horizon h4 with thrust fault traces. Contour interval is at 100 m. (b) Fault heave and shortening value, (c) Fault dip angle for selected thrusts, (d) forelimb dip and interlimb angle, and (e) Depth to fold crest of horizon h4.

Figure 13. Fold-related shortening along strike for (a) Fold train A and (b) Fold train B. Difference between shortening (solid gray line) and summed heave (dotted gray line) provides rough estimate of shortening accommodated by folding (dash-dotted black line). Maximum values of fold-related shortening, c. 1 km, appears to be an upper limit where folding can accommodate shortening at horizon h4.

Figure 14. (a) Total fault heave and (a) Total shortening across fold trains A and B. Summed fault heave and shortening for individual fold trains are displayed for comparison. Total fault heave and total shortening present generally linear gradients, implying kinematic coherence between the fold trains.

Figure 15. A model for the evolution of fold-thrust structures. (a) Early stage of fold-thrust belt development. At this stage, individual structure segments are geometrically isolated. Increased strain is distributed between closely neighboring structures. (b) Hard linkage of aligned segments is established as structures laterally propagate. Increased fold strain is distributed in linkage site due to decreased fault displacement. (c) Imbricate thrusts occur on former linkage site to compensate for diminished fault displacement. Soft linkage site is developed as non-aligned structures approach. (d) Imbricate thrusts dominantly accommodate shortening on linked segments.

Accumulated fold strain on soft linkage site between non-aligned structures forms deflection in fold hinge. See text for further explanation.

Supplemental Material captions

Supplemental Material 1a. High-resolution image of seismic section a-a' without author's interpretation (equivalent to left panel of Figure 10a).

Supplemental Material 1b. High-resolution image of seismic section a-a' with author's interpretation (equivalent to right panel of Figure 10a).

Supplemental Material 2a. High-resolution image of seismic section b-b' without author's interpretation (equivalent to left panel of Figure 10b).

Supplemental Material 2b. High-resolution image of seismic section b-b' with author's interpretation (equivalent to right panel of Figure 10b).

Supplemental Material 3a. High-resolution image of seismic section c-c' without author's interpretation (equivalent to left panel of Figure 10c).

Supplemental Material 3b. High-resolution image of seismic section c-c' with author's interpretation (equivalent to right panel of Figure 10c).

Supplemental Material 4a. High-resolution image of seismic section d-d' without author's interpretation (equivalent to left panel of Figure 10d).

Supplemental Material 4b. High-resolution image of seismic section d-d' with author's interpretation (equivalent to right panel of Figure 10d).

Supplemental Material 5a. High-resolution image of seismic section e-e' without author's interpretation (equivalent to left panel of Figure 10e).

Supplemental Material 5b. High-resolution image of seismic section e-e' with author's interpretation (equivalent to right panel of Figure 10e).

Supplemental Material 6a. High-resolution image of seismic section f-f' without author's interpretation (equivalent to left panel of Figure 10f).

Supplemental Material 6b. High-resolution image of seismic section f-f' with author's interpretation (equivalent to right panel of Figure 10f).

Supplemental Material 7a. High-resolution image of seismic section g-g' without author's interpretation (equivalent to left panel of Figure 10g).

Supplemental Material 7b. High-resolution image of seismic section g-g' with author's interpretation (equivalent to right panel of Figure 10g).

Supplemental Material 8a. High-resolution image of seismic section h-h' without author's interpretation (equivalent to left panel of Figure 10h).

Supplemental Material 8b. High-resolution image of seismic section h-h' with author's interpretation (equivalent to right panel of Figure 10h).

Figure 1

Click here to download high resolution image

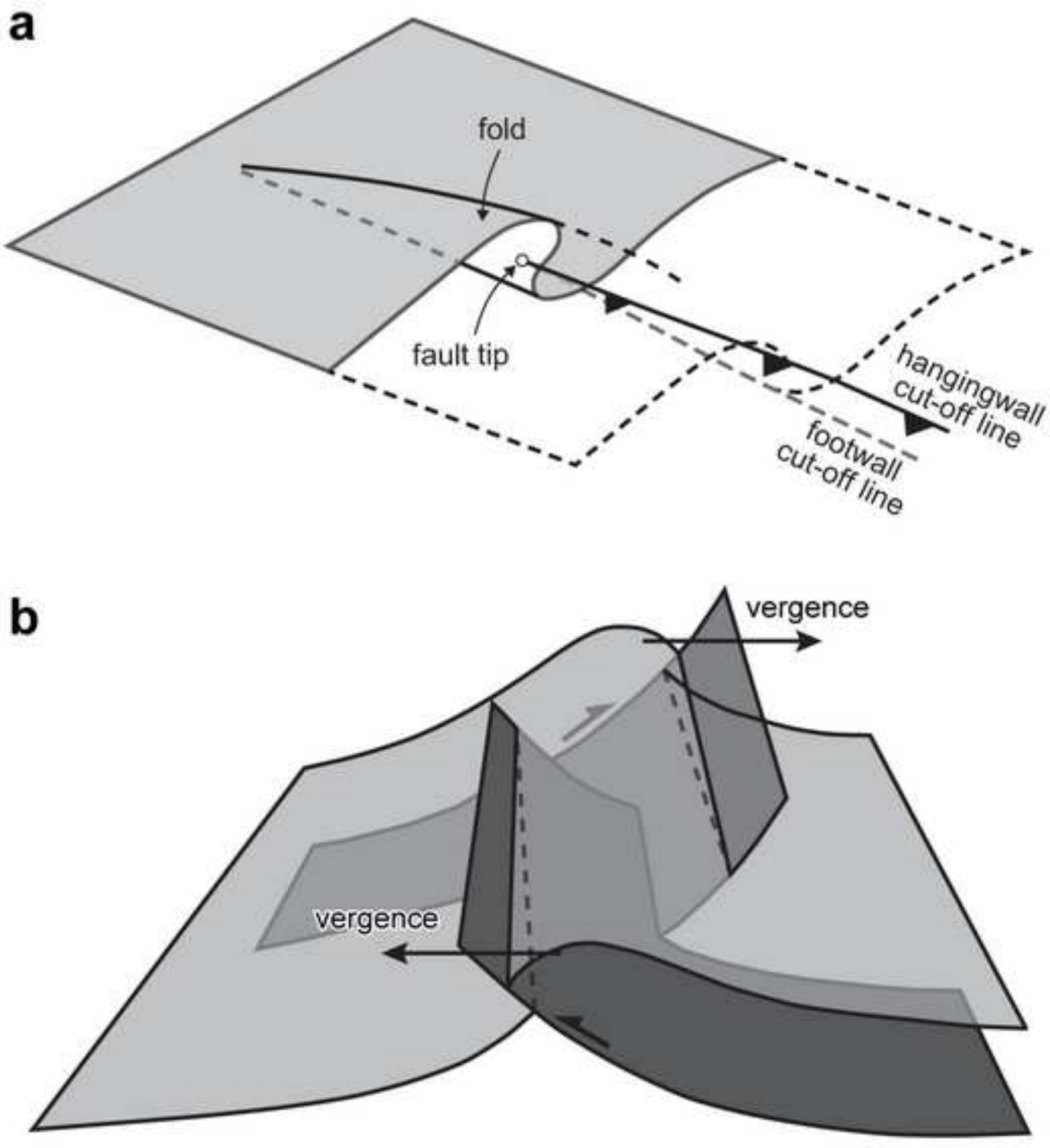

Figure 2

Click here to download high resolution image

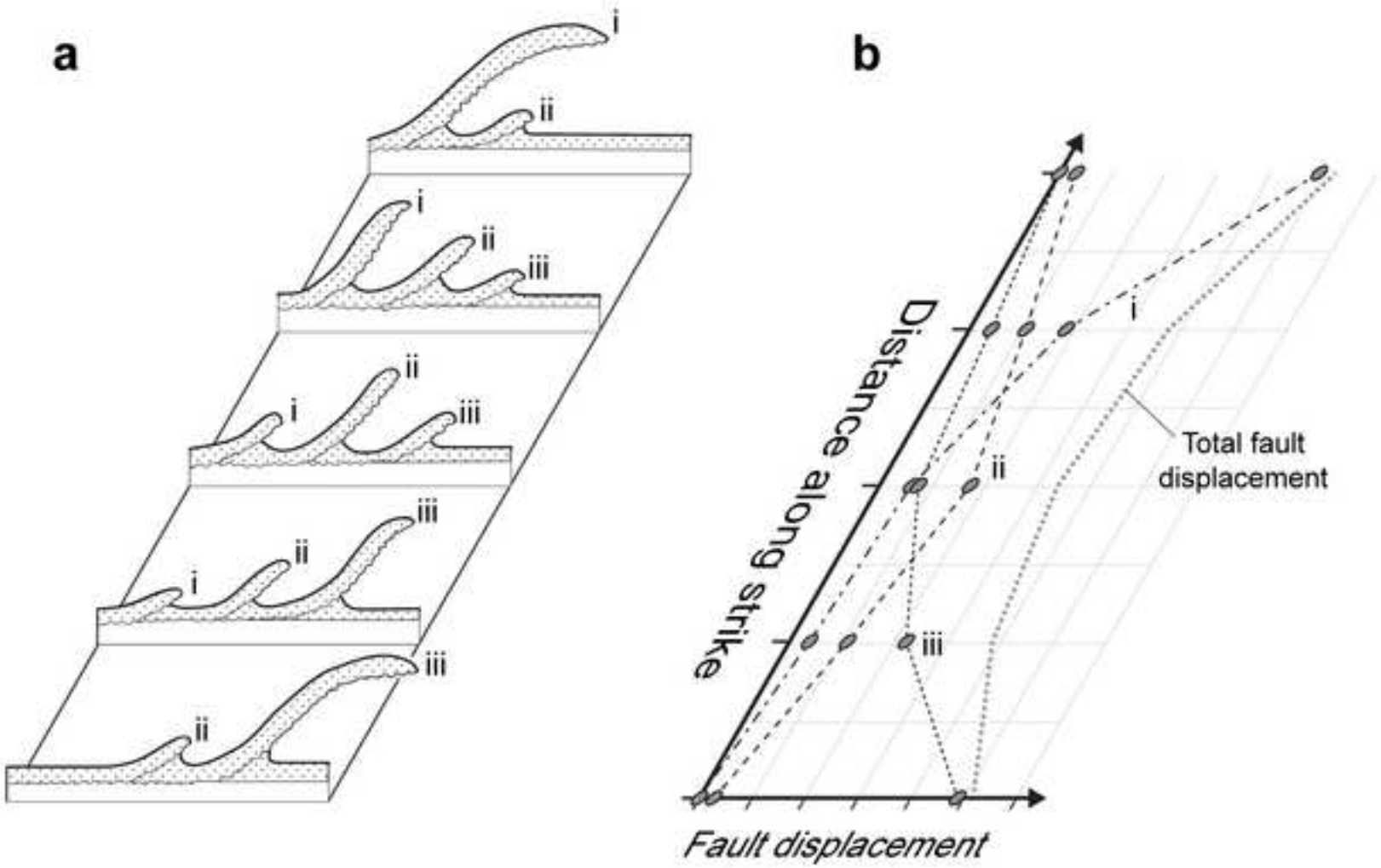

Figure 3

Click here to download high resolution image

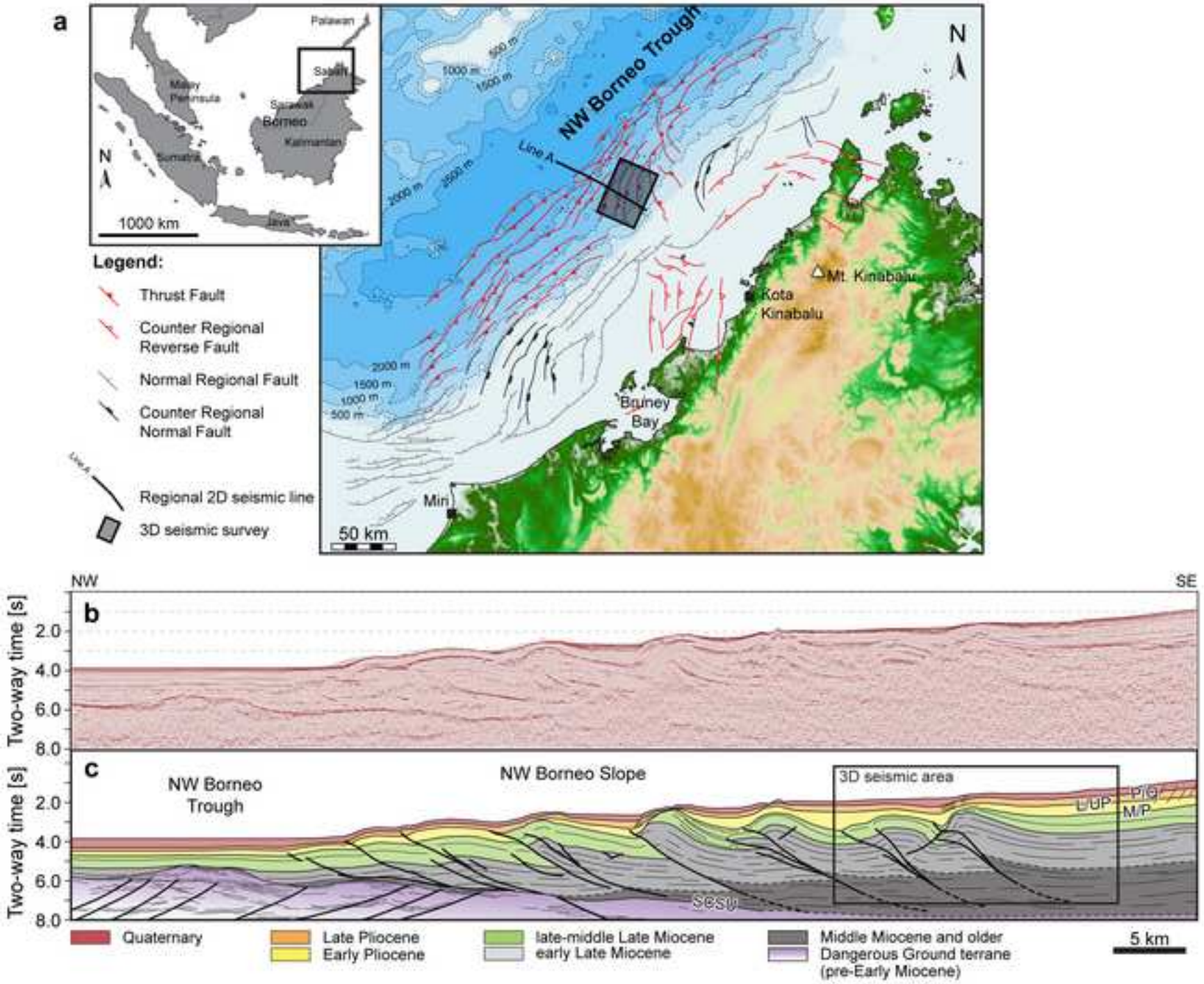

Figure 4

Click here to download high resolution image

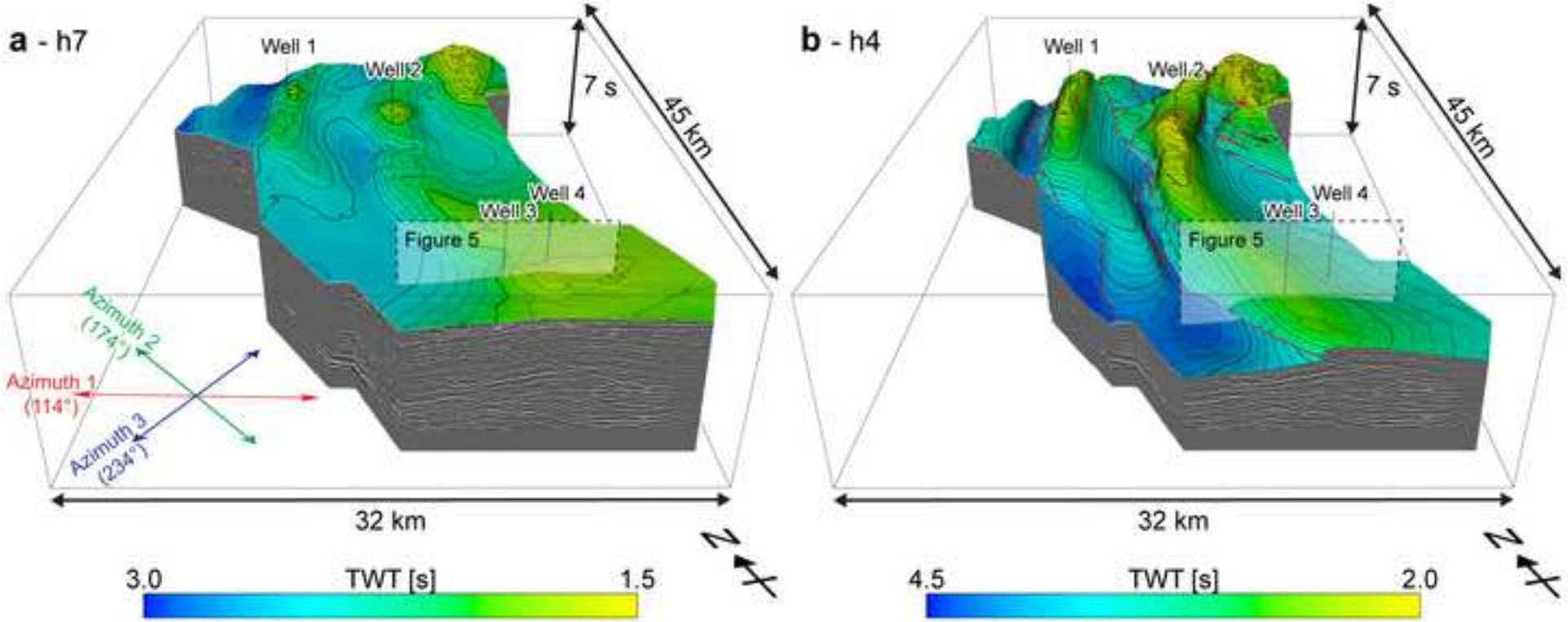

Figure 5

Click here to download high resolution image

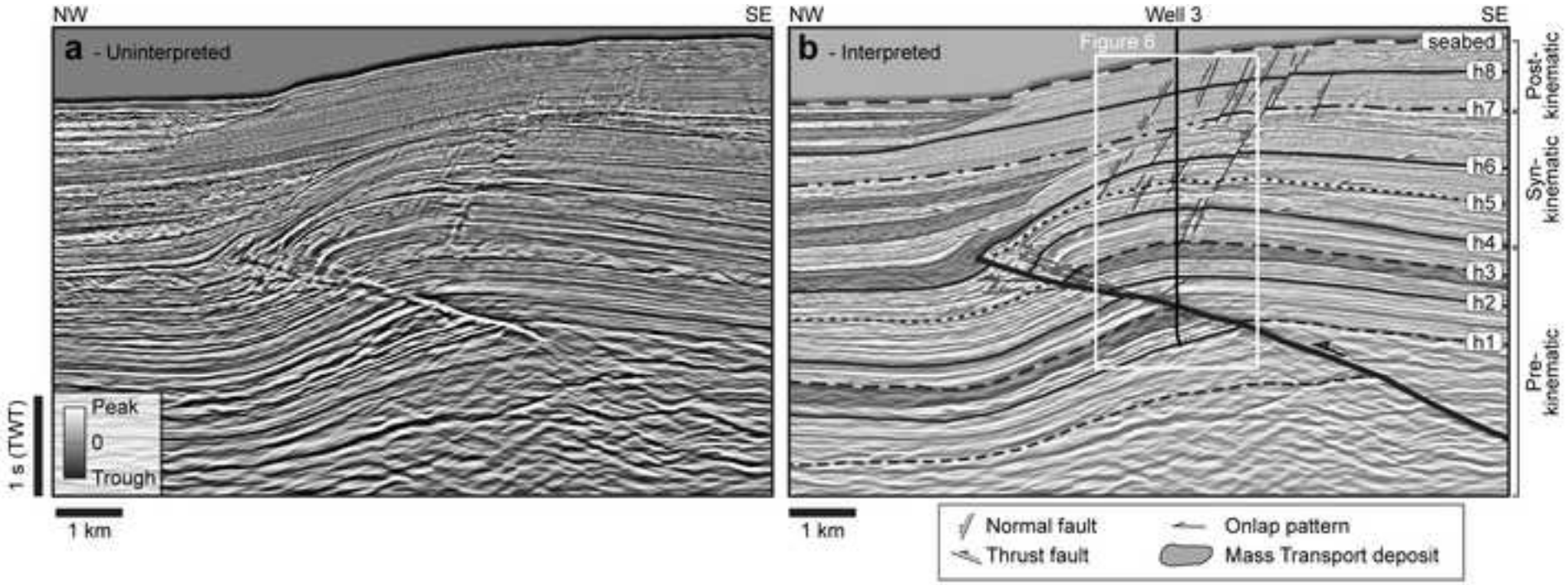

Figure 6

Click here to download high resolution image

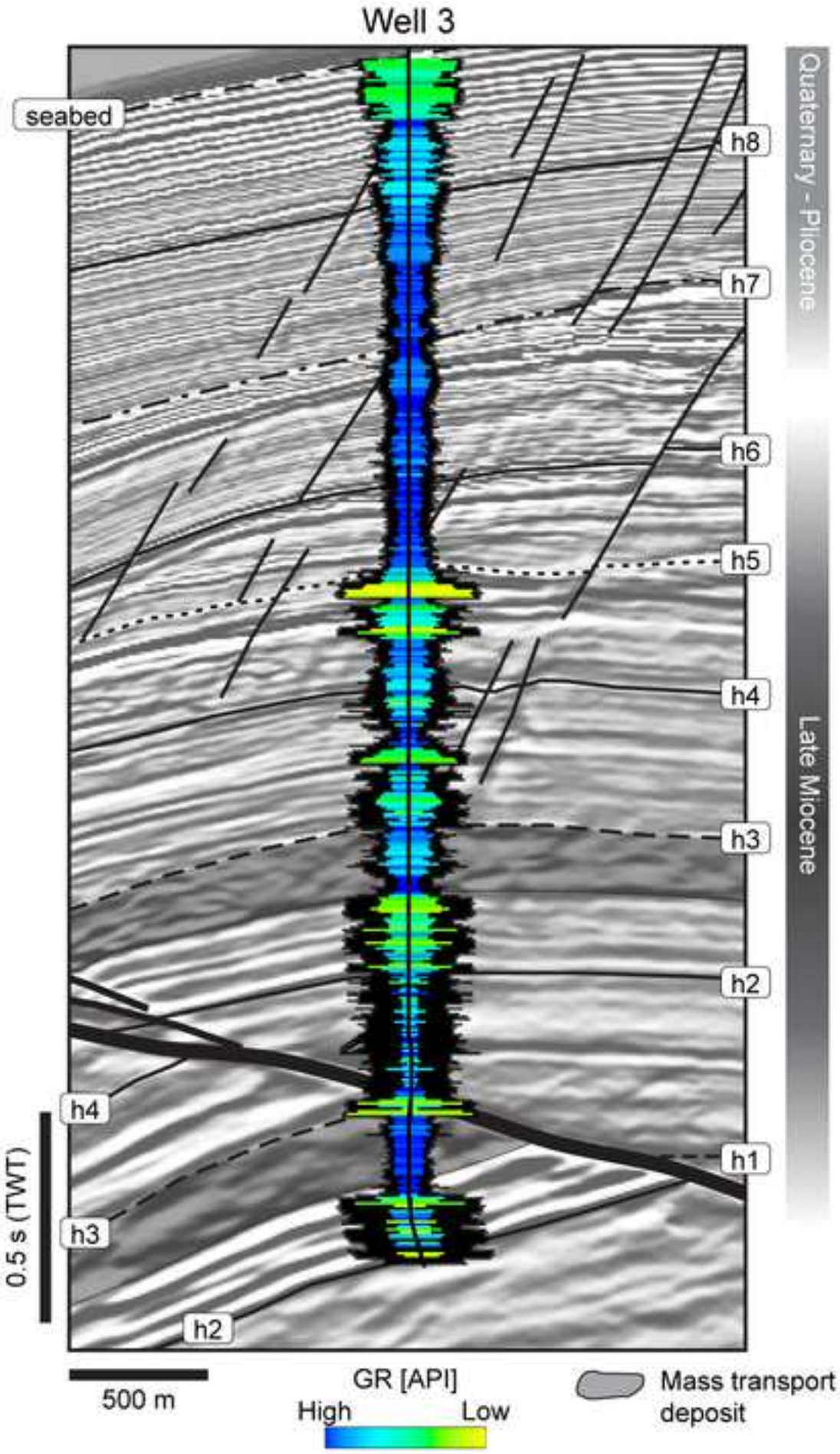

Figure 7

Click here to download high resolution image

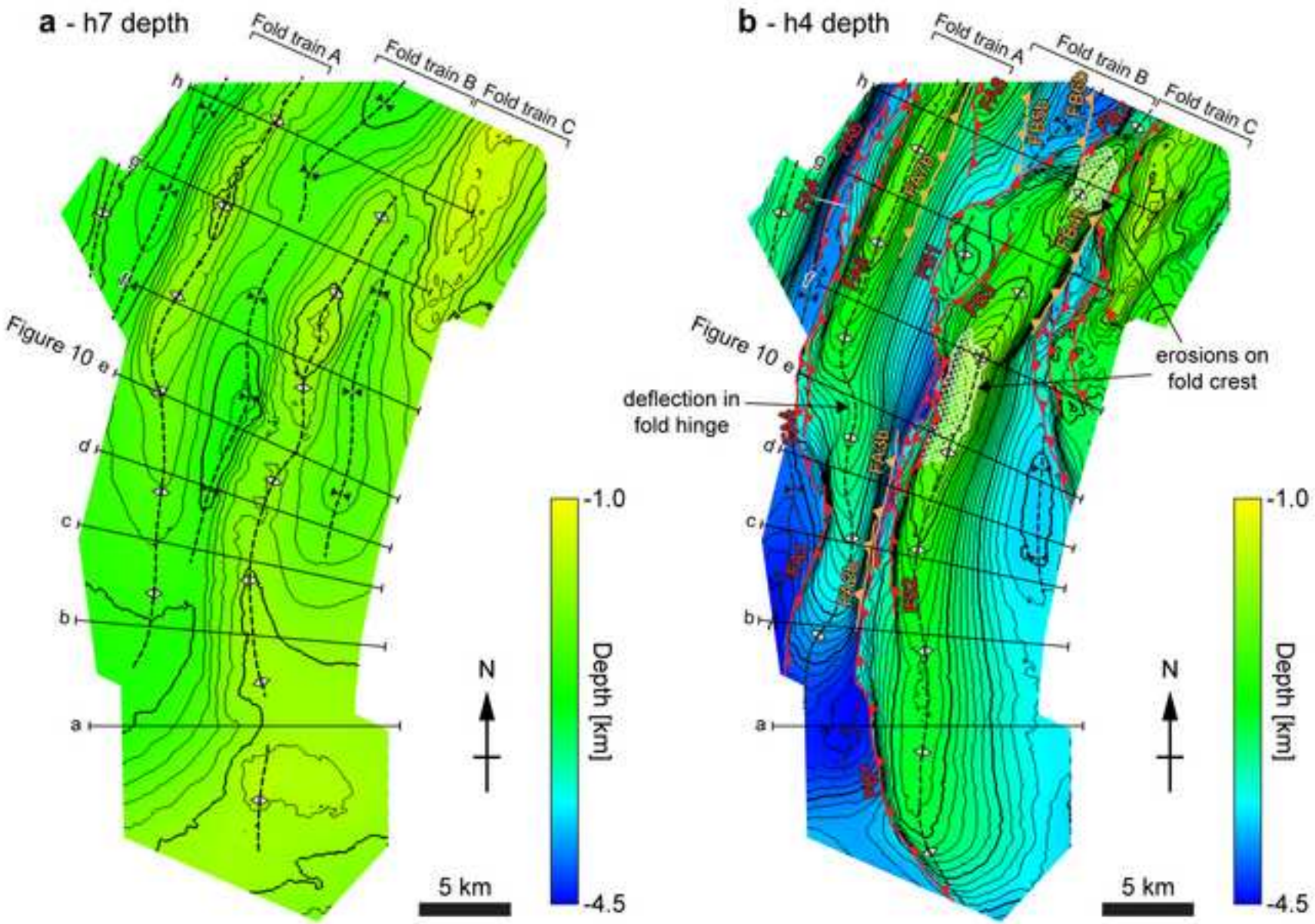

Figure 8

Click here to download high resolution image

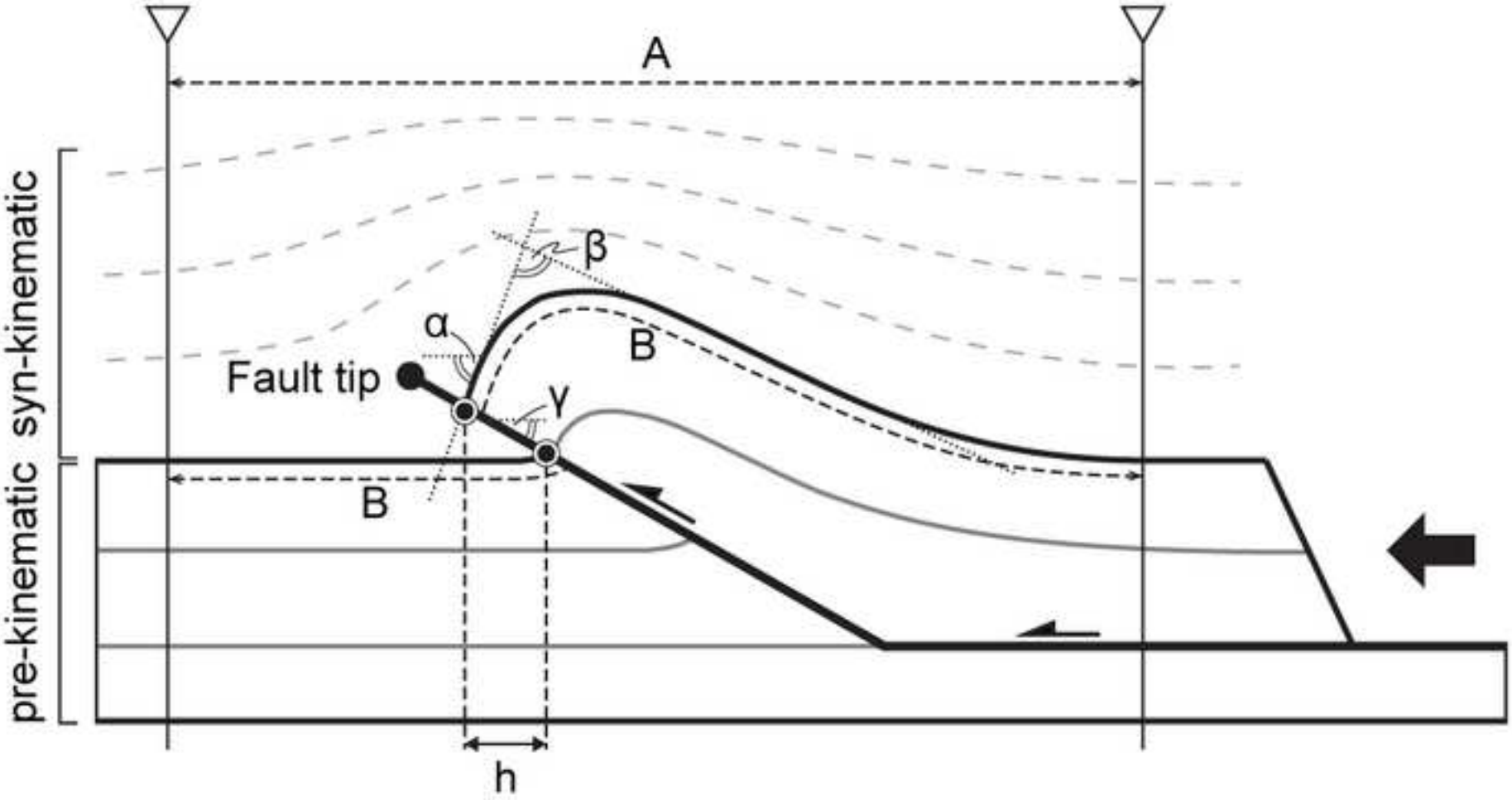

Figure 9

Click here to download high resolution image

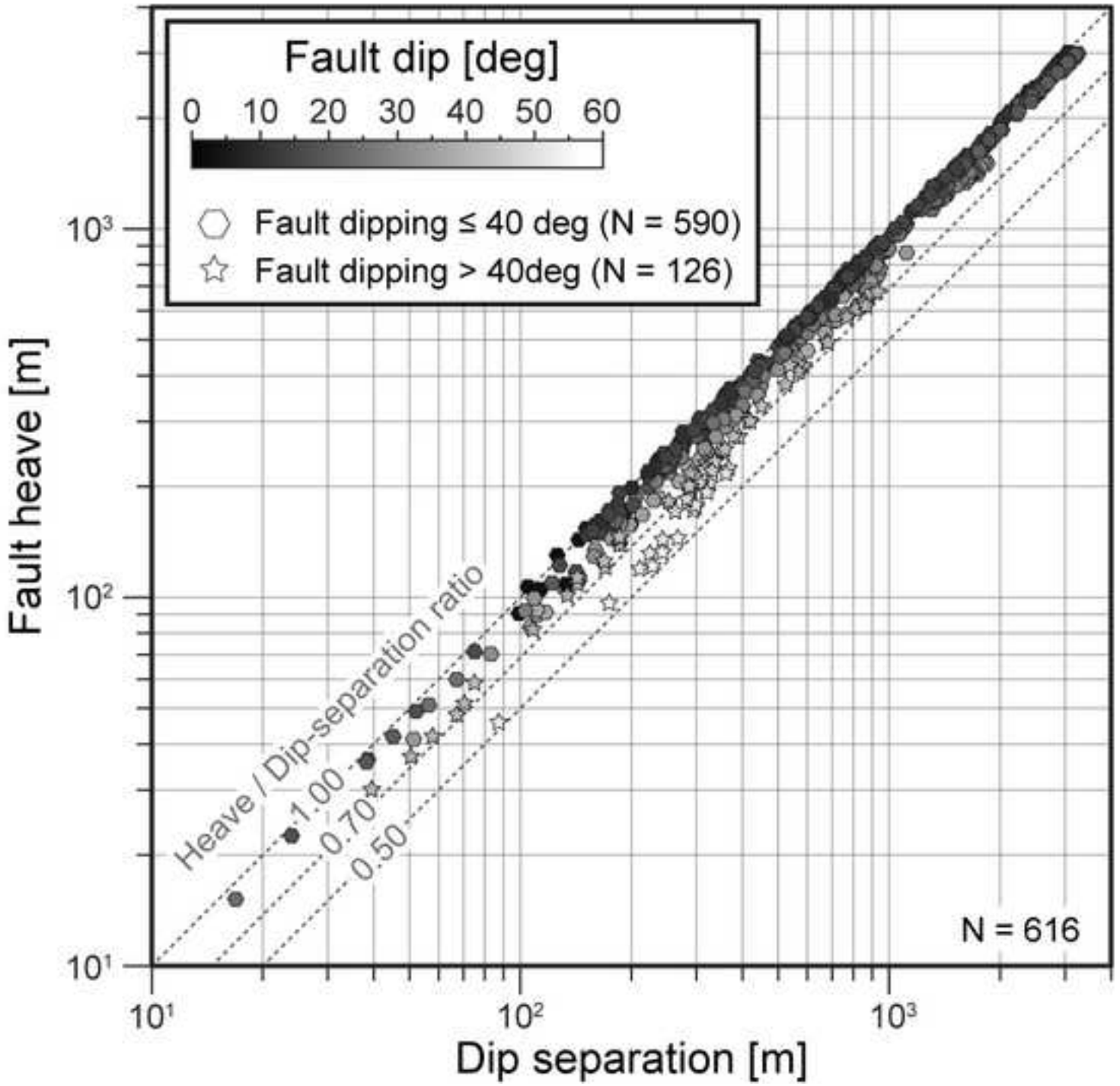

Figure 10-1

Click here to download high resolution image

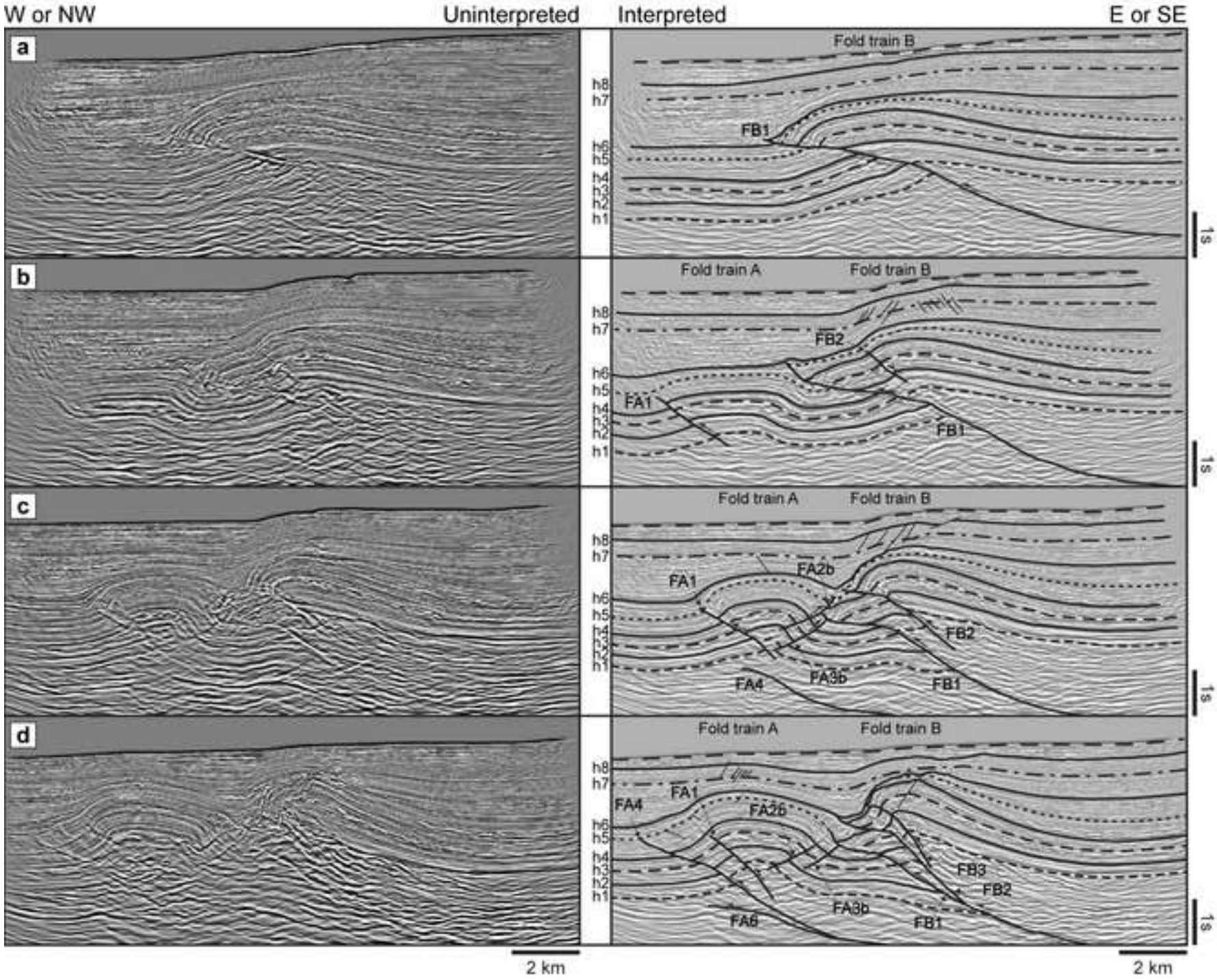

Figure 10-2

Click here to download high resolution image

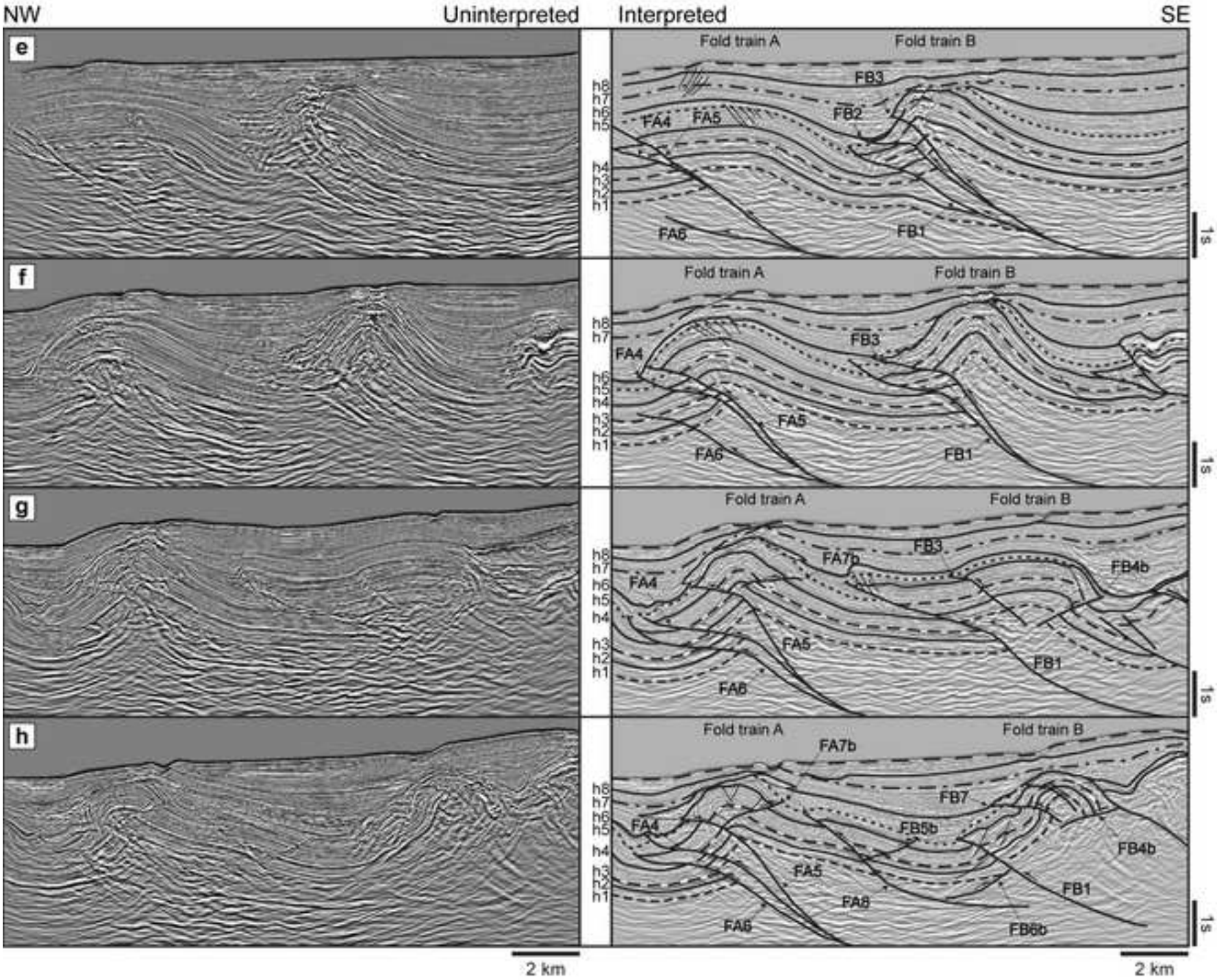

Figure 11

Click here to download high resolution image

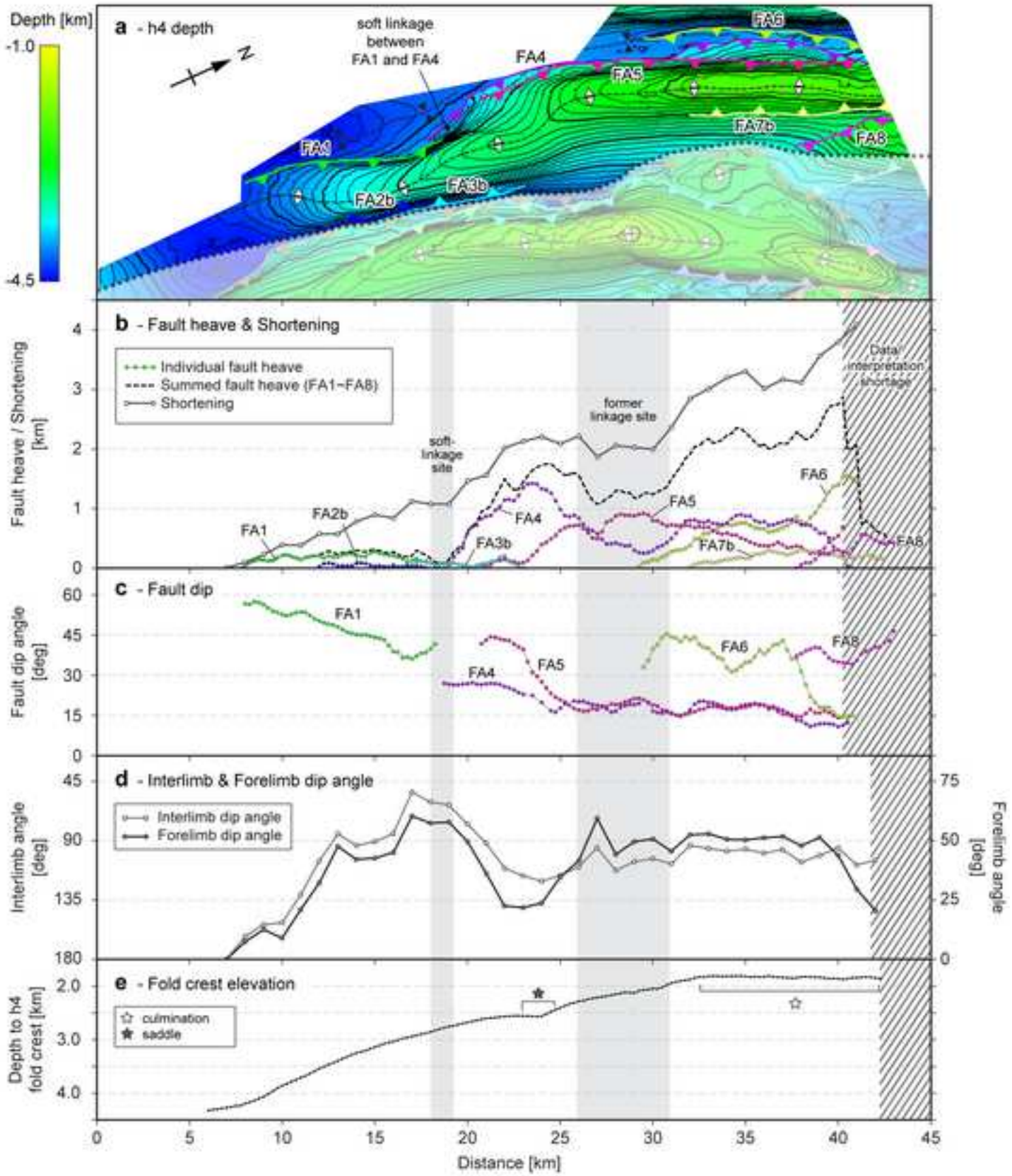

Figure 12

Click here to download high resolution image

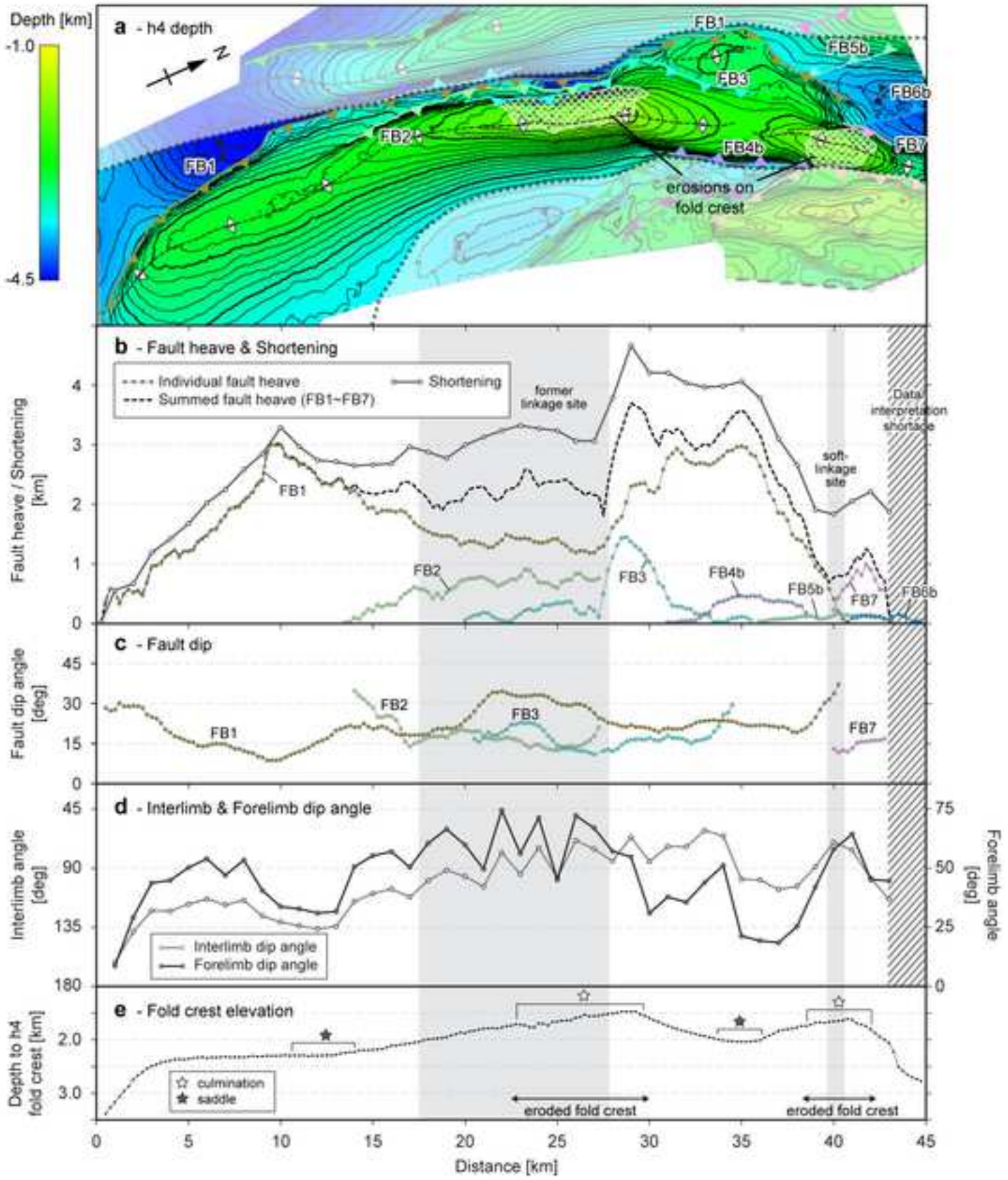

Figure 13

Click here to download high resolution image

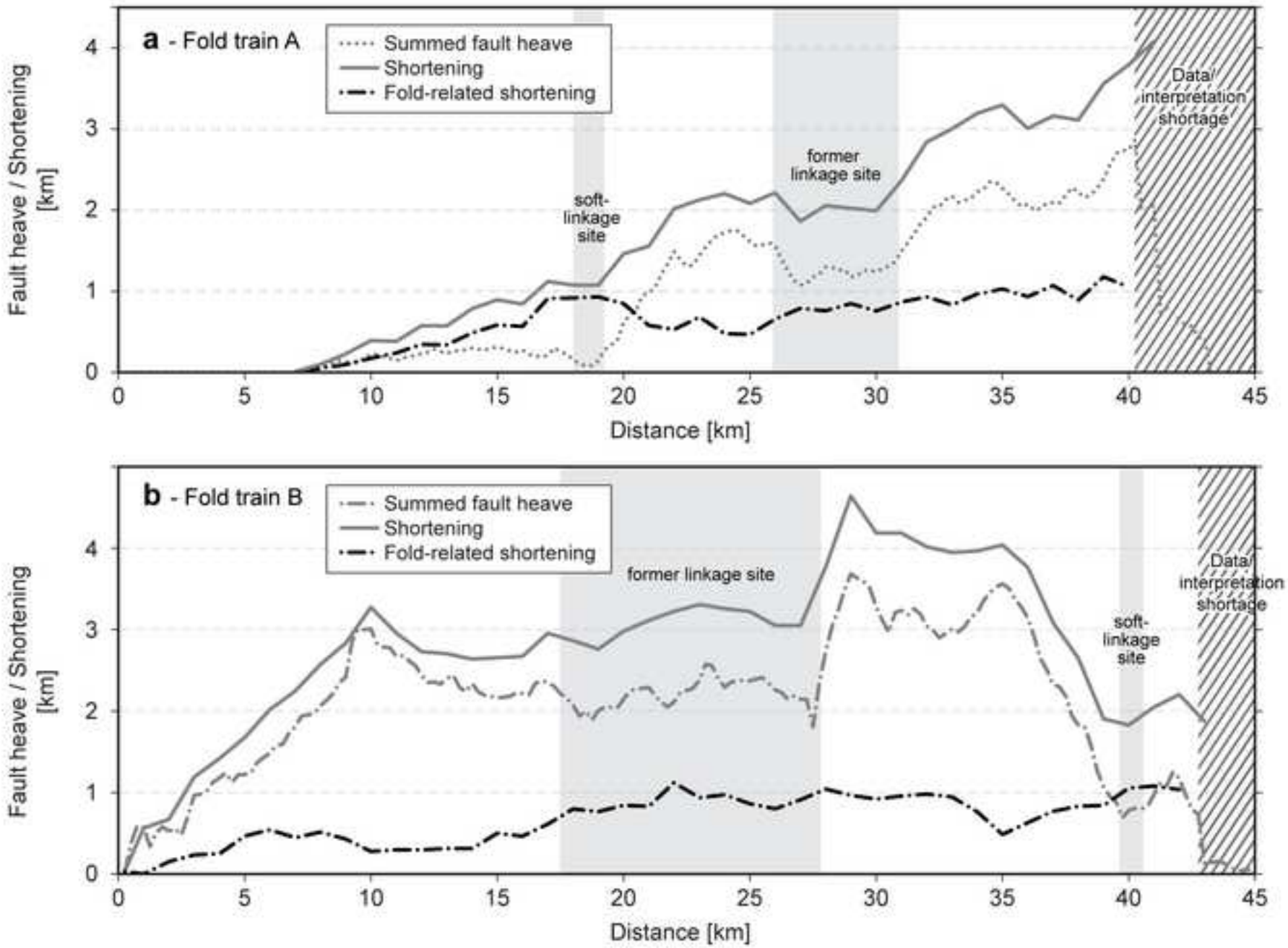

Figure 14

Click here to download high resolution image

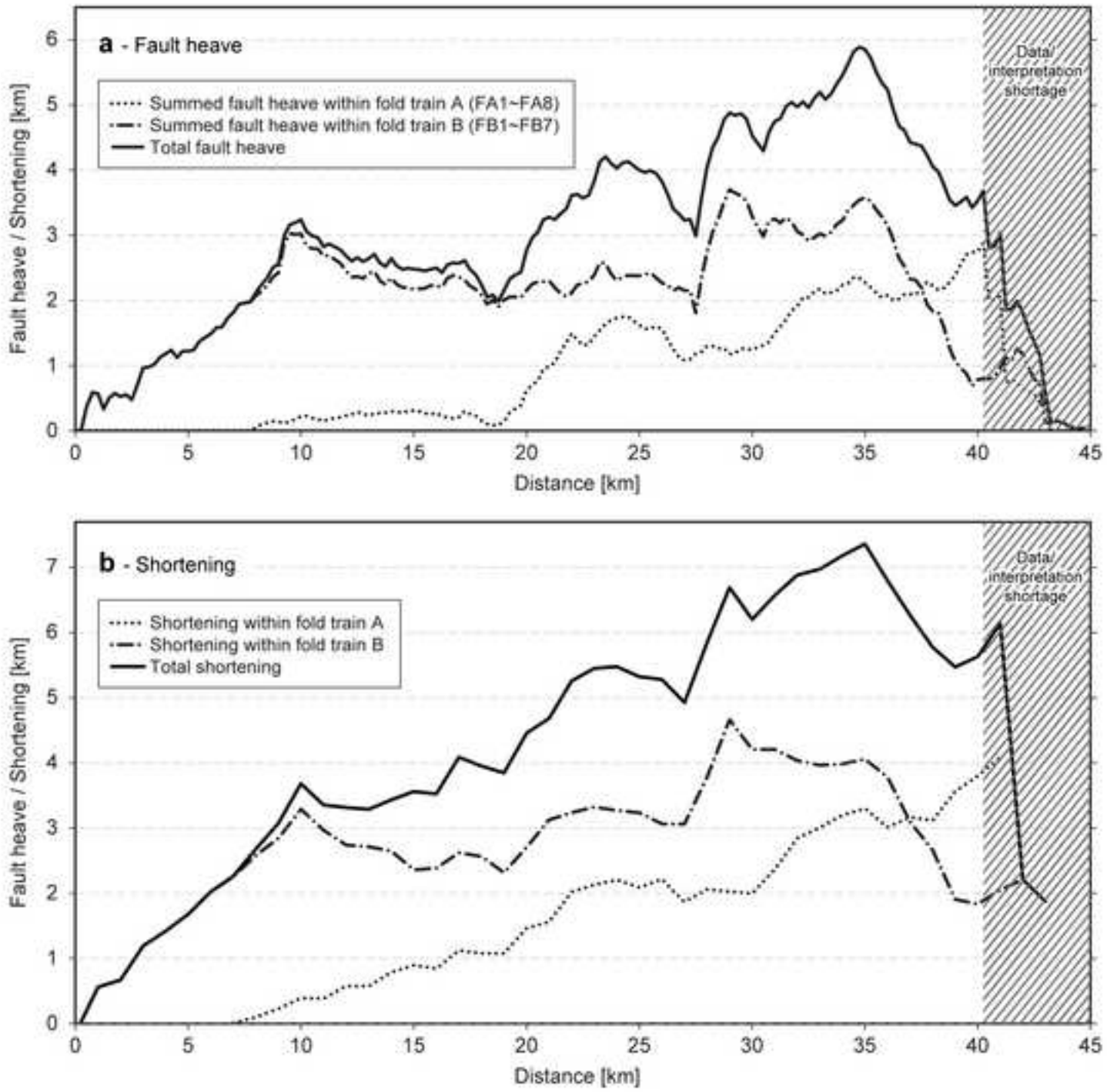

Figure 15

Click here to download high resolution image